Journal of Phase Equilibria and Diffusion
ASM INTERNATIONAL

Influence of 5 at.%Al-additions on the FCC to BCC phase transformation in CrFeNi concentrated alloys

Journal:	*Journal of Phase Equilibria and Diffusion*
Manuscript ID	JPED-21-03-2507.R2
Manuscript Type:	Research Article
Date Submitted by the Author:	15-Aug-2021
Complete List of Authors:	Zuo, Xiaojing; KU Leuven, Dept. of Materials Engineering Miotti Bettanini, Alvise; UCLouvain, iMMC - IMAP Hilhorst, Antoine; UCLouvain, iMMC-IMAP Jacques, Pascal; UCLouvain, iMMC - IMAP Moelans, Nele; KU Leuven, Dept. of Materials Engineering
Keywords:	phase field modeling, experimental kinetics, phase transformation, high entropy alloys, diffusion, AlCrFeNi

Influence of 5 at.%Al-additions on the FCC to BCC phase transformation in CrFeNi concentrated alloys

X. Zuo[1]*, A. Miotti Bettanini[2], A. Hilhrost[2], P.J. Jacques[2], N. Moelans[1]

[1] Dept. of Materials Engineering, KU Leuven, Kasteelpark Arenberg 44 Bus 2450, Leuven, 3001, Belgium

[2] Institute of Mechanics, Materials and Civil Engineering, UCLouvain, B-1348 Louvain-la-Neuve, Belgium

In the context of the recent developments in the field of high entropy alloys (HEAs), CrFeNi based alloys with the addition of Al have gained significant attention due to their interesting combination of mechanical properties and corrosion resistance, enabling an even wider range of applications for HEAs. A key feature of this system is the co-existence of multiple phases such as body centered cubic (BCC) and face centered cubic (FCC) phase, which significantly enhances the mechanical performance of the alloy. However, despite the ongoing research efforts, an in-depth study of the effect of Al on the phase transformation kinetics in this system is not yet available, which undermines the design of effective heat treatments, curbing the optimization of microstructures and properties. In this work, the influence of 5 at.%Al addition on the interdiffusion behavior and phase transformation kinetics from FCC to BCC phase at 700 ℃ is studied by experiments and state-of-the-art phase field simulations. The kinetics of BCC precipitation are observed experimentally through the sequential characterization of samples heat treated up to 11 days. 2D phase field (PF) simulations of the growth and coarsening of BCC-precipitates in a dual-phase BCC/FCC system are performed on the same alloy system. Experimental observations reveal that the growth of BCC is greatly enhanced by the addition of Al to the ternary CrFeNi system. This result is consistent with findings from the phase field simulation. PF results show that the

gradients of the diffusion potentials and interdiffusion mobilities are increased in the case of Al addition, which explains the significant increase of the phase transformation rate from FCC to BCC. Finally, the cross terms in multi-component diffusion equations are found to significantly affect the evolution of the phases. These findings demonstrate the need of multicomponent models to fully understand the complex interdiffusion behavior in high and medium entropy alloys to foster the design of these materials.

1.Introduction

In recent years, a new paradigm in alloy design has emerged. Compositionally complex alloys, better known as High Entropy Alloys (HEAs), are a promising class of materials that consists of multi-principal element alloys with typically 3 to 5 elements in equal or near-equal atomic concentration. Surprisingly, it was found that several multicomponent alloys form relatively simple single phase or dual phase systems despite the difference in chemical affinity of the forming elements. HEAs are considered viable choices for a wide range of applications in view of their excellent mechanical and functional properties, which can be tailored to the specific application through the adjustment of the chemical composition[1–4]. Among popular systems, excellent cryogenic mechanical properties are reported for the 5-elements CrMnFeCoNi [5,6]. More recently, it was found that the simpler ternary CrCoNi [7–9] alloy displays outstanding strength and toughness even superior to the more complex 5-elements systems. In both cases, a drastic increase in the strength and ductility is attributed to the activation of the twinning mechanism as the temperature is lowered to liquid nitrogen (77K).

The $Al_xCoCrFeNi$ system has recently gained lots of interest due to the ability to fine tune the microstructure with Al addition and thermo-mechanical processing. Between $x = 0.1$ and $x = 0.3$, the system is FCC and displays mechanical twinning resulting in excellent impact toughness, ductility, and strength [10–16]. By further increasing the Al content, the system becomes a dual phase BCC/FCC alloy at equilibrium [17,18]. Careful processing of these dual phase alloys can result in excellent mechanical properties [19,20]. A peculiarity of this system is the precipitation from the FCC matrix of hard BCC_B2

(ordered) phase rich in Al and Ni as the Al content of the alloy is increased [17,21–24]. The ordered BCC_B2 intermetallic phase appears at about 11 at.% of Al in the Al_x-CoCrFeNi system in the as-cast microstructure [25]. It was found that during the solidification, Al and Ni segregate to the interdendritic regions, where they stabilize a disordered BCC_A2 phase, which will further decompose in BCC_B2 (ordered) and BCC_A2 (disordered) phases. Aging at high temperature progressively transforms the structure from FCC to BCC_B2, which correlates with an increase of the hardness of the alloy[26,27]. A thermodynamic assessment of the AlCoCrFeNi system [28,29] confirmed that Al addition stabilized both BCC_A2 and BCC_B2 phase while increasing the amount of Cr in the system stabilizes only the disordered BCC_A2 phase at the expense of the ordered BCC_B2 phase.

While interesting from a research perspective, HEA systems containing Co will not prove cost-effective in the short term due to the very high price and strategic issues of obtaining a viable source of raw Cobalt [30]. Thus, Co-free systems like AlCrFeNi have been recently investigated [31–35] and excellent compressive strength was observed in AlxCrFeNi (where x=9-13). This system features a dual phase structure composed of disordered BCC_A2 rich in Fe and Cr and ordered BCC_B2, rich in Ni and Al. Dong et al[33] found excellent tensile properties for an AlCrFe2Ni2 alloy in the as-cast conditions. The very peculiar microstructure consists of needle-like FCC, BCC_A2 and BCC_B2. The same microstructure was recently investigated with ultra-high resolution TEM characterizations by Eshed et al. [35] in the as-cast and homogenized conditions. During prolonged homogenization at 750°C they observed the partial dissolution of the Cr-rich disordered BCC phase and the subsequent precipitation of ordered B2 phase rich in Al and Ni. These different studies confirmed the thermodynamic assessment of the Al-CrFeNi system carried out by Tian et al [34]. In all systems reviewed here, the addition of Al leads to the stabilization of BCC-type structures at the expense of the FCC structures, thus opening interesting pathways for the optimization of duplex microstructures in a similar manner as already established for Fe-based alloys in the case of the duplex stainless steels.

Optimization of microstructure through heat treatments requires the knowledge of the effect of alloying elements on the kinetics of phase transformations. Lin et. al[27] found that progressive aging of Al0.5CoCrFeNi alloy with 11 at.% of Al leads to the precipitation of Al, Ni-rich BCC phase into the FCC matrix, with a consequent increment of the hardness of the alloy. On the other hand, a systematic study of the BCC precipitation in the cost-effective Co-free AlCrFeNi and CrFeNi systems is still lacking. Due to the very complex interactions in multicomponent systems, computational methods can greatly contribute to gain insight in the mechanisms driving the phase transformation. Phase Field (PF) method has been employed widely to study the mechanisms controlling phase transformations and microstructure evolution [36–38]. Microstructure evolution during phenomena, such as spinodal decomposition[39], solidification [40,41], precipitate growth and dissolution [42,43] and intermetallic phase morphology evolution [44] are well studied by PF simulations. For this reason, the PF method is applied to model the BCC/FCC phase evolution in the (Al)CrFeNi system in this work. However, limited literature [45–47] was reported on PF simulation for quaternary alloy systems, mainly due to the high complexity of using thermodynamic and kinetic information of multicomponent alloys into a PF model.

As reported, the FCC phase provides good ductility and BCC phase shows good strength. Therefore, to reach a good compromise between these two mechanical properties, the alloy studied in this paper is designed to be in the two-phase region. Based on thermodynamic calculation carried out with Thermo-Calc v.2020 software using the TCHEA2 database, it was decided to study the effect of 5 at.% Al addition on the FCC to BCC phase transformation during isothermal heat treatment at 700°C of equimolar CrFeNi alloy. Experimental observations show that BCC growth is significantly enhanced in the presence of Al. This behavior is then also studied using multicomponent phase-field simulations that consider the effect of Al addition on the growth rate of BCC phase from FCC matrix. The understanding of the thermodynamic and kinetic driving force could lead to optimization of the chemical composition in order to promote the precipitation of strengthening phase such as the BCC particles. Moreover, the role of the cross terms in the diffusion equation, i.e., the fact that a gradient in composition of one of the elements can drive diffusion of the other elements, in determining the

growth kinetics and microstructure evolution will be studied based on the phase field simulations in this paper.

2. Methods

2.1. Experimental procedure

200 grams cylindrical ingots (diameter = 11 mm) of one ternary equimolar CrFeNi alloy and one quaternary Al-CrFeNi alloy were manufactured by arc-melting high purity (> 99.9%) elements under a protective argon atmosphere. Each ingot was remelted at least four times to ensure chemical homogeneity. After casting, a piece of each ingot was cut for ICP chemical analysis. The ingots were then hot-rolled at 900 °C down to 6 mm thickness and annealed at 1000 °C for 30 minutes. The ingots were then cut into several pieces perpendicular to the rolling direction. Each slice was put in a quartz capsule filled with argon gas to protect the material from oxidation. The aging heat treatment was performed at 700 °C for times ranging from 24 hours to 270 hours (~11 days). The samples were then ground and polished following standard metallographic practices. Each sample was first mechanically ground with SiC papers, then polished down to 1 µm diamond paste followed by final polishing with 0.03 µm OPS-A suspension. Microstructural characterization was performed on unetched surfaces by Scanning Electron Microscopy (SEM) equipped with back-scattered electrons (BSE) detector. X-ray diffraction (XRD) with Cu radiation operated at 30 kV and 30 mA was performed to characterize the crystallography of the constitutive phases of the microstructure. Finally, the volume fraction of each phase was calculated by quantitative image analysis on SEM micrographs using the open-source ImageJ software.

2.2 Phase Field model description and parameters determination

2D PF simulations of the growth and coarsening of BCC-precipitates in a dual phase BCC/FCC system were conducted for Al 5 at.%-CrFeNi alloys and Al-free CrFeNi alloy. The system temperature and pressure were kept constant, which is consistent with experimental conditions. The thermodynamic (Gibbs energies) and kinetic (Mobilities) information, which is needed in the PF model were extracted from databases assessed according to the CALPHAD method [48]. For the Gibbs energies of the BCC and FCC phases, polynomial functions were fitted to the Gibbs-energy data computed for the two-phase region using the TCHEA2 Thermo-Calc database. To find the BCC/FCC two-phase region in the quaternary system, pseudo-ternary isothermal sections of the Al_xCrFeNi phase diagram, with $x = 0.01, 0.03, 0.05, 0.07$ in mole fraction, were extracted as shown in Fig. 1. The colored areas correspond to the two-phase regions for each fixed x amount of Al. The local mole fractions of Al, Cr, and Fe are represented by the variables x_{Al}, x_{Cr} and x_{Fe}. The mole fraction of Ni is obtained as x_{Ni}=1-x_{Al}-x_{Cr}-x_{Fe}. As shown in Fig. 1, when the Al mole fraction gradually increases from 0.01 to 0.07, the BCC/FCC two-phase area shrinks significantly. From this diagram, it was decided to fit the Gibbs energy polynomials over the composition range of 0.01< x_{Al} <0.08, and 0.01< x_{Cr} <0.97, 0.01< x_{Fe} <0.5, accordingly, which is slightly larger than the colored region in the phase diagram to ensure the two-phase area is fully included.

To assess the effect of 5 at.% Al addition on the BCC/FCC phase transformation, we simulated such phase transformation in a ternary Al-free CrFeNi alloy and a quaternary Al 5at%-CrFeNi alloy. Two cases with different initial compositions are considered for each alloy. In a first case (EQ), the equilibrium compositions (as obtained from Thermo-Calc calculations) are assumed in both BCC and FCC phase in the initial microstructure. In the second case (NEQ), an initial microstructure is taken with the thermodynamic equilibrium composition for the BCC phase, but a composition deviating from the equilibrium composition for the FCC phase. The initial concentrations as considered in the simulations for both cases are listed in

Table 2.

Table 1 Measured ICP chemical composition (mole fraction) of the ternary CrFeNi and quaternary Al-CrFeNi

Alloy	Cr	Al	Fe	Ni
CrFeNi	0.34	0	0.34	0.32
Al-CrFeNi	0.32	0.05	0.32	0.31

Table 2 Initial compositions of BCC and FCC phase taken in the simulations for the Al-CrFeNi and Al-free CrFeNi alloy systems for the two cases discussed in the text, namely assuming equilibrium compositions in both the BCC and FCC phase (EQ), and assuming equilibrium composition in BCC phase only and a deviation from the equilibrium composition in FCC phase (NEQ).

Alloys	Cases	Phases	Cr	Al	Fe	Ni
CrFeNi		Overall	0.33	0	0.33	0.34
	(equilibrium, EQ)	BCC	0.85911		0.13166	0.00923
		FCC	0.25121		0.35954	0.38926
	(nonequilibrium, NEQ)	BCC	0.85911		0.13166	0.00923
		FCC	0.33		0.33	0.34
Al-CrFeNi	(equilibrium, EQ)	Overall	0.3166	0.05	0.3166	0.3167
		BCC	0.83419	0.00075	0.15739	0.00767
		FCC	0.15991	0.06491	0.36480	0.41038
	(nonequilibrium, NEQ)	BCC	0.83419	0.00075	0.15739	0.00767
		FCC	0.3166	0.05	0.3166	0.3167

Kim et al. [49] introduced a general type of PF model to study microstructure evolution for binary alloys, *i.e*, the so-called KKS model. Later, Kim et al. [50,51] further extended the KKS model into multicomponent multiphase systems. Moelans [52,53] introduced a new type of interpolation function allowing quantitative PF modeling for multiphase systems, which guarantees thermodynamic consistency not only in grains and at interfaces but also in multi-junctions. Within the context of the

multiphase-field approach in the PF model, the different grains or phases are identified using different phase field variables representing individual grains or phases in the alloy system. In this model, we assign a single non-conserved phase field variable η_{BCC} to represent BCC phase, and two non-conserved phase field variables η_{FCC1} and η_{FCC2} to present two grains of FCC phase, to study the effect of the presence of a grain boundary (GB) on the growth and shape of BCC precipitates. η_i=1 ($i =$ FCC1, FCC2, or BCC) indicates the presence of phase i on a particular location in the simulation system, while η_i=0 indicates the complete absence of phase i. At the interface between the two phases or grains, the non-conserved phase field variables show a diffuse transition between 0 and 1.

The total free energy F of the system is formulated as a function of the non-conserved order parameters representing the different phases η_i and the local molar fraction values, x_{Al}, x_{Cr} and x_{Fe}, as:

$$F = \int_V \frac{k}{2}\sum_i (\nabla\eta_i)^2 + mf_0(\eta_i) + \sum_i h_i \frac{G^i}{V_m} dV, \quad (1)$$

where i=FCC1, FCC2 or BCC and G^i are the Gibbs energy for each phase. The first two terms in the integral represent the interfacial free energy, with f_o a fourth-order Landau polynomial of the three order parameters according to Moelans et al. [52].

$$f_0 = \sum_{i=1}^{3}\left[\frac{1}{4}\eta_i^4 - \frac{1}{2}\eta_i^2\right] + \sum_{i=1}^{3}\sum_{j>i}^{3} 1.5\eta_i^2\eta_j^2 + 0.25. \quad (2)$$

Further, the h_i in Eq. (1) are functions used to interpolate between the bulk phase properties, such as Gibbs energy density and diffusion mobilities, at the diffuse interfaces between different phases. For multiphase systems, it is introduced in the following format, according to Moelans. [53]

$$h_i = \frac{\eta_i^2}{\sum_{i=1}^{3}\eta_i^2} \quad (3)$$

The evolution equations for the mole fractions are derived starting from the following equations, which ensure mass conservation:

$$\frac{1}{V_m}\frac{\partial x_k(\mathrm{x,t})}{\partial t} = -\nabla \mathrm{j}_k = \sum_{l=1}^{3} \nabla M_{kl}(\mathrm{x,t})\nabla\tilde{\mu}_l(\mathrm{x,t}) \quad (4)$$

with $x_k(x, t)$ the mole fraction of component k and j_k [(mol)/(m²·s)] the flux of component k. The diffusion potential $\tilde{\mu}_k$ is defined in Eq.(8). As done in many phase-field models, we assume that the molar volume has a constant value V_m = 10^{-5} m³/mol. Taking into account volume effects in a

phase-field model for solid-solid phase transformations would also require including elastic effects, which will be discussed in future work.

When the evolution of the BCC precipitates under the effect of only the bulk diffusion is studied, the mobilities M_{kl} are taken as:

$$M_{kl} = \sum_{i=1}^{3} h_i(\eta) M_{kl}^{iN} \quad (5)$$

with the M_{kl}^{iN} the elements of the mobility tensor for phase i and assuming a number-fixed reference frame with $N = N_k$ the dependent component.

When the effect of the presence of a GB and grain boundary diffusion on the evolution of BCC precipitates is studied, the expression of the mobility is taken as:

$$M_{kl} = \sum_{i=1}^{3} h_i M_{kl}^{iN} + \sum_{i=1}^{3} \sum_{j>i}^{3} M_{gb} \eta_i^2 \eta_j^2 \quad (6)$$

In this case, M_{gb} can be related to the experimentally measurable grain boundary diffusion coefficient D_{gb}, or mobility $M_{gb,exp}$ using the relation[44]:

$$M_{gb} = 3\left(\frac{D_{gb}}{\partial^2 f^{FCC}/\partial x_k^2}\right)\left(\frac{\delta_{gb}}{l}\right) = 3M_{gb,exp}\left(\frac{\delta_{gb}}{l}\right) \quad (7)$$

with δ_{gb} the physical width of the grain boundary, and l the width of the diffuse interface assumed in the phase-field model, which is related to the parameters *k* and *m* through Eq. (16), as explained further in the text.

The M_{kl}^{iN}[unit: (mol^2)/(J·m·s)] are interdiffusion mobilities in the FCC and BCC phases. For each phase, the interdiffusion mobilities M_{kl}^{iN} in Eq. (5) and Eq. (6) are defined using the composition dependent expression $M_{kl}^{iN} = \sum_{k=1}^{3}(\delta_{kl} - x_l)\sum_{m=1}^{3}(\delta_{mn} - x_n)L_{mk}$, with $L_{mk} = \frac{x_m}{V_m} M_m^i$ for $m = k$ and $L_{mk} = 0$ for $m \neq k$, M_m^i the atomic mobilities of the 4 elements for each phase and N represent the dependent component (in this case, Ni). In this work, the atomic mobilities M_m^i are assumed to be independent of composition. Their values were calculated using Thermo-Calc with the MobNi4 mobility database and assuming the equilibrium composition of each phase. They are listed in Table 3. It was verified that the atomic mobilities are indeed almost constant over the concentration region considered in the simulations. The GB mobility plays a vital role in phase evolution, however, there is no literature reporting GB mobility values for high entropy alloys. The grain boundary mobility is

related to the boundary diffusion coefficient. In this paper the GB mobility coefficient is taken as $\tilde{M}_{gb} = max(\tilde{M}_k^i)$. ($\tilde{M}_k^i$ is taken as $M_k^i/(\frac{x_c^2}{RTt_c})$: the values are 0.2253 and 185 for FeCrNi and Al-FeCrNi respectively), The corresponding atomic mobility values are given in Table 3.

Table 3 Atomic mobilities M_m^i [unit: (mol·m2)/(J·s)] used in PF simulation.

Phases	M_{Cr}	M_{Al}	M_{Fe}	M_{Ni}
BCC_CrFeNi	2.1037e-25		1.1142e-25	1.221e-25
FCC_CrFeNi	2.4245e-23		7.2702e-24	2.7851e-23
BCC_Al-CrFeNi	5.5619e-25	2.2992e-20	2.0404e-25	2.1302e-25
FCC_Al-CrFeNi	5.3388e-23	1.932e-22	4.5403e-23	8.5663e-23

Following the KKS approach, phase compositions x_k^i are introduced. They are determined at each position, such that for each of the components, the diffusion potential is equal in the coexisting phases, giving the following set of equations:

$$\begin{aligned}
\frac{\partial G^{FCC1}}{\partial x_{Al}^{FCC1}} &= \frac{\partial G^{FCC2}}{\partial x_{Al}^{FCC2}} = \frac{\partial G^{BCC}}{\partial x_{Al}^{BCC}} = \tilde{\mu}_{Al} \\
\frac{\partial G^{FCC1}}{\partial x_{Cr}^{FCC1}} &= \frac{\partial G^{FCC2}}{\partial x_{Cr}^{FCC2}} = \frac{\partial G^{BCC}}{\partial x_{Cr}^{BCC}} = \tilde{\mu}_{Cr} \\
\frac{\partial G^{FCC1}}{\partial x_{Fe}^{FCC1}} &= \frac{\partial G^{FCC2}}{\partial x_{Fe}^{FCC2}} = \frac{\partial G^{BCC}}{\partial x_{Fe}^{BCC}} = \tilde{\mu}_{Fe}
\end{aligned} \tag{8}$$

where G^{FCC1}, $G^{FCC2}$and G^{BCC} are the Gibbs energy densities of the two grains in FCC phase and BCC phase respectively, which have the unit: J/mol. The $\tilde{\mu}_k$ (unit : J/mol) are the diffusion potentials of the independent components. Moreover, the overall mole fractions x_k (the variables for which the diffusion Eq. (4) are solved) are related to these phase composition variables using the interpolation function h_i, as:

$$x_k = \sum_{i=1}^{3} h_i x_k^i \tag{9}$$

giving three more equations needed to determine the set of phase composition variables x_k^i.

Since better stability is obtained in the simulations when using reduced parameters, the PF equations above were nondimensionalized by introducing the following dimensionless quantities:

$$x = x_c\tilde{x}, t = t_c\tilde{t}, G = G_c\tilde{G}, m = m_c\tilde{m}, \quad (10)$$

where x_c, t_c, m_c, and G_c are characteristic scales of the variables. Their values are given in Table 4. We assume the characteristic energy G_c=RT, and the dimensionless diffusion mobility is obtained from Eq.(11),

$$\tilde{M}_{kl} = \frac{M_{kl} \cdot RT \cdot V_m \cdot t_c}{(x_c)^2} \quad \tilde{M}^i_m = \frac{M^i_m \cdot RT \cdot t_c}{(x_c)^2} \quad (11)$$

Using Eq. **Error! Reference source not found.**, Eq. **Error! Reference source not found.** becomes:

$$\frac{\partial x_k}{\partial t} = \sum_{l=1}^{3} \nabla \tilde{M}_{kl} \nabla \left[h_i \frac{\partial \tilde{G}^i}{\partial x_l} \right]. \quad (12)$$

The time evolution of the non-conserved order parameters is calculated according to Allen-Cahn equations, namely as $\frac{\partial \eta}{\partial t} = -L_\eta \frac{\delta F}{\delta \eta}$. For the Gibbs free energy of the form of Eq. **Error! Reference source not found.**, the following evolution equations for the order parameters representing FCC and BCC phase can be obtained:

$$\frac{\partial \eta_i}{\partial t} = -L_\eta \left({\eta_i}^3 - \eta_i + 3\eta_i \sum_{j>i}^{3} {\eta_j}^2 - k\nabla^2\eta_i + \sum_i \frac{\partial h_i}{\partial \eta_i} f^i \right) \quad (13)$$

With the substitution of the dimensionless variables in Eq.**Error! Reference source not found.**, Eq. **Error! Reference source not found.** becomes:

$$\frac{\partial \eta_i}{\partial \tilde{t}} = -L_\eta t_c m_c \tilde{m} \left[{\eta_i}^3 - \eta_i + 3\eta_i \sum_{j>i}^{3} {\eta_j}^2 - \frac{k}{m_c \tilde{m} x_c^2} \nabla^2 \eta_i + \sum_i \frac{\partial h_i}{\partial \eta_i} \frac{\tilde{G}_i G^c}{m_c \tilde{m} V_m} \right]$$

(14)

The relationship between simulation parameters and dimensional values are:

$$\tilde{L}_\eta = t_c L_\eta m_c \tilde{m}, \tilde{k} = \frac{k}{m_c \tilde{m} x_c^2}, \; G_c = V_m m_c \tilde{m}. \quad (15)$$

In this model, boundaries between phases are considered as diffuse interfaces with finite width. The model parameters m and k are related to the interfacial free energy δ and diffuse interface width l as:

$$\delta = \frac{\sqrt{2}\sqrt{mk}}{3}, \; l = 2\sqrt{2}\frac{\sqrt{k}}{\sqrt{m}}. \quad (16)$$

from which the model parameters m and k are then obtained as:

$$k = \frac{3}{4} l\delta, m = \frac{6\delta}{l}. \quad (17)$$

The kinetic coefficient L should be taken according to Eq. (18) to obtain diffusion-controlled interface migration in the PF model, as derived in [53]:

$$L_\eta = \frac{\sqrt{2}mg}{kI_\phi \zeta}. \quad (18)$$

where $\zeta^{FCC/BCC} = \Delta c M^{-1} \Delta c = \sum_{k=1}^{C-1} (x_{FCC,eq,k} - x_{BCC,eq,k}) \sum_{m=1}^{C-1} (\mathrm{M}_{km}^{FCC/BCC} V_m)^{-1} (x_{FCC,eq,k} - x_{BCC,eq,k})$. The numerically evaluated values for I_ϕ and g are chosen according to Ref. [54], the values used in our simulations are listed in Table 4.

The dimensional and characteristic values considered are listed in Table 4, the non-dimensional values for the calculation are acquired correspondingly as: $\frac{G_c}{V_m m_c \tilde{m}} = 1$, $\tilde{m} = 1$, $\tilde{k} = \frac{k}{\mathbb{m}_c \tilde{\mathbb{m}} {x_c}^2} = 4.636$. The kinetic Eq. (12) and (14) and the auxiliary Eq. (8) and (9) were solved using the finite element method (FEM) in Multiphysics Object-Oriented Simulation Environment (MOOSE) Framework [55]. Adaptive time stepping is used.

The molar factions x_k and order parameters η_i are obtained at every time step as the solutions of the diffusion and PF equations. In the simulation, the parameters used for 2-Dimensional (2-D) simulations are listed in Table 4.

Table 4 Material and numerical parameters used in the 2D PF simulation.

	Parameters	Function	Value
Dimensional values	Δx, Δy	----	1.0 e-9 m
	V_m	----	1.0 e-5 $m^3 \cdot mol^{-1}$
	δ	----	0.5 $J \cdot m^{-2}$
	L_y / N_y	----	1.0 e-7m / 100
	L_x / N_x		(1.0 e-7m / 100) (2.0 e-7m / 200)
	l^{int}	$10\Delta x$	10.0 e-9 m
	k	$\frac{3}{4} l\delta$	3.75 e-9 $J \cdot m^{-1}$

	m	$\frac{6\delta}{l}$	3e8 J·m^{-3}
	g	----	0.471405
	I_ϕ	----	0.5
	L_η	$\frac{\sqrt{2}mg}{kI_\phi\zeta}$	3.0057 e-11 m^{3}J^{-1}s^{-1}
Characteristic values	x_c / t_c	----	1.0 e-9 m / 1 s
	m_c	RT/V_m	8.089 e8 J·m^{-3}
	G_c	RT	8.089 e3 J·mol^{-1}
Dimensionless values	$\tilde{m}$	----	1
	$\tilde{k}$	$\frac{k}{m_c\tilde{m}{x_c}^2}$	4.636
	$\tilde{L}_{\eta\_}alloy1$	$t_cL_\eta m_c\tilde{m}$	0.0098
	$\tilde{L}_{\eta\_}alloy2$	$t_cL_\eta m_c\tilde{m}$	0.024

3. RESULTS

3.1. Experimental results

Table 1 shows the chemical composition of the ternary equimolar CrFeNi and quaternary Al-CrFeNi (Al = 5 at.%) after casting. At the aging temperature of 700°C, CALPHAD thermodynamic calculations predict a mole fraction of BCC phase equal to 24 mol.% and 15 mol.% for the quaternary Al-CrFeNi and ternary CrFeNi systems, respectively.

The experimental observations confirm the presence of a dual-phase microstructure for all the different investigated experimental conditions. Fig. 2 (a-h) shows SEM micrographs of the microstructures obtained after each heat treatment. Both materials retain part of the as-cast microstructures featuring elongated grains (dendrites) with inter-dendritic precipitation, as still visible in Fig. 2 (a-e). This feature is rather large in the quaternary alloy. BCC particles appear darker with the BSE detector, suggesting that this phase is constituted of elements with an average atomic number lower than the brighter matrix phase. The precipitation in the ternary CrFeNi takes place primarily at GB, as visible in Fig. 2 (a-d).

Moreover, the chemical contrast achieved with BSE outlines a chemical gradient along the GB, which appears brighter than the matrix. On the other hand, aging at 700°C the quaternary Al-CrFeNi alloy leads to the precipitation of a network of a secondary phase that decorates the interdendritic regions, as shown in Fig. 2 (e-f). For longer aging times, this is soon replaced by more fragmented precipitation of elongated lenticular particles that do not present the same continuity or network-like morphology seen on shorter aging times, as visible in Fig. 2 (g-h). After 270 hours at 700 °C, the darker phase is homogeneously dispersed in the matrix of the quaternary Al-CrFeNi alloy. Moreover, experimental characterizations indicate that the darker precipitates consist mainly of elongated lenticular particles (intragranular Widmanstatten plates or needles). This morphology becomes dominant after 168 h at 700 °C in the quaternary Al-CrFeNi system. On the contrary, BCC precipitation in ternary CrFeNi alloy is mainly idiomorph, maintaining an equiaxed shape throughout the heat treatments.

Quantitative analysis of SEM micrographs reveals the evolution of phase fraction of BCC precipitates for both alloys investigated. Fig. 3 shows the area fraction of the secondary phase for the quaternary Al-CrFeNi and ternary CrFeNi alloys. In the first case (blue dotted line), the area fraction increases sharply, reaching about 20 vol.% after 200 h of isothermal heat treatment at 700°C. On the other hand, the evolution for the ternary alloy (red, solid line) is considerably slower. The heat treatment does not produce any substantial effect in the first 72h, during which the volume fraction of BCC phase remains constant. This is followed by a small increment up to ~5 vol.% after 270 h at 700°C. Characterizations of the different phases by x-ray diffraction confirm the results obtained by SEM micrographs characterizations. XRD diffraction spectra for 0h, 72h and 270h holding time at 700°C are shown in Fig. 4 and Fig. 5 for CrFeNi and Al-CrFeNi alloys, respectively. An analysis of the XRD spectra indicates strong reflections corresponding to a FCC phase of space group Fm3m and a secondary reflection corresponding to disordered BCC of space group Im3m in both samples. Fig.4 shows reflections corresponding to a BCC phase at t = 0h. The intensity of these peaks is increasing as

the sample is heat treated at 700°C for t = 72 h and t= 270 h, which well agrees with the SEM characterization showing a steep increase of the BCC volume fraction in the AlCrFeNi alloy.

On the contrary, no BCC reflections are detected at t = 0h in the CrFeNi (Fig. 5), despite the presence of this phase being confirmed by SEM characterization. This may occur when the volume fraction of BCC phase is below the detection threshold of the XRD measurement. A reflection (2Theta = 44°) corresponding to the BCC phase is detected in the CrFeNi sample heat treated for t = 270h, which confirms the presence of disordered BCC-type phase in the ternary alloy.

3.2. Simulation Results

3.2.1. Effect of Al on the growth of the precipitates

Growth and coarsening (without grain boundary effect) of BCC precipitate in an FCC matrix in the quaternary Al-CrFeNi and ternary CrFeNi alloys was studied following the evolution of a microstructure with initially 50 BCC precipitates and an initial radius of 4 nm distributed randomly in the FCC matrix of size 100 nm × 100 nm. Fig. 6 shows the evolution with time of precipitate area in the two systems for two different cases with different initial composition of the FCC phase as listed in Table 2. At the beginning of the simulations, the BCC precipitate area fraction experiences a sudden drop, also for the cases with equilibrium composition in the initial microstructure, due to the curvature effect. The drop in area fraction for these small precipitates is exaggerated in the phase-field model since the initial particle size is smaller than the diffuse interface width. It should be considered as an artificial initialization effect in the simulations. The drop is however immediately followed by growth of the remaining precipitates and an increase of the BCC precipitate area fraction, which is a realistic effect. In all cases, the growth is very fast in the initial 4.8 hours; the average growth rates are 236, 517, 235 and 341 (nm^2 / hour) for Al-CrFeNi (EQ), Al-CrFeNi (NEQ), CrFeNi (EQ) and CrFeNi (NEQ), respectively. This initial stage, characterized by a fast growth is followed by a second stage of slower growth which tends asymptotically towards the thermodynamic equilibrium fraction.

When starting from the initial condition with equilibrium composition in both the BCC and FCC phase, the evolution of the BCC precipitate area as a function of time is comparable for both the ternary CrFeNi and quaternary Al-CrFeNi systems. This is because the system starts from a condition close to the equilibrium condition, and the driving force for the evolution of the microstructure mainly comes from the curvature effect. With the same initial geometry for both alloys, the driving force is thus almost the same. However, when starting from a non-equilibrium composition (same with experiment) in the FCC matrix (NEQ), a drastically different growth rate is obtained for CrFeNi and Al-CrFeNi. At 14 hours, the precipitate area fraction in Al-CrFeNi is about 5 at.% larger than for CrFeNi and more than two times larger than for both alloys when considering initial equilibrium conditions.

3.2.2. Effect of the cross-diffusion terms

The diagonal terms (i.e. M_{ii}) in Eq. (4) are called the main diffusion coefficients, the off-diagonal terms (i.e. M_{ij}) are called the cross term diffusion coefficients. Each cross term relates the concentration evolution of solute i to the concentration gradient of solute j (e.g.,: the cross terms contributing to the diffusion flux of Cr for AlCrFeNi alloy are $\nabla M_{CrFe}(\mathrm{x,t})\nabla\tilde{\mu}_{Fe}(\mathrm{x,t})$ and $M_{CrAl}(\mathrm{x,t})\nabla\tilde{\mu}_{Al}(\mathrm{x,t})$. To investigate the effect of the cross terms upon the kinetic growth of the precipitates and the microstructure, additional simulations were carried out for the cases assuming initial equilibrium concentrations in both the BCC and FCC phase (cases EQ in table 2), and for both the Al-CrFeNi and CrFeNi alloys. The evolution of the same initial microstructures was simulated using the PF model with and without cross terms in the diffusion equation. Fig.7(a) shows the area fraction of the BCC precipitates as a function of time, with the black and red lines representing the growth for Al-CrFeNi and the blue and purple lines representing the growth for CrFeNi, with and without cross terms in the simulation. It is clear from the graph that the cross terms affect the slopes of the growth curves, which indicates that the cross interactions have a significant effect on the evolution process of the BCC precipitates. The maximum absolute deviation(|area fraction obtained with cross term-area fraction obtained without cross term|) on the BCC area fraction at a certain time, between the model with and without cross terms, is 1.61% for Al-CrFeNi and 0.93% for CrFeNi. For this system, the effect is thus

larger for the alloy with Al added than for the ternary system. The final area fractions are not affected by the cross terms, since the cross terms only affect the evolution.

Fig. 7(b) shows the evolution of BCC precipitates at time frames of (a) 9172.59 s and (b) 9188.18 s resulting from the PF simulation with and without the cross terms for Al-CrFeNi and starting from the initial microstructure with equilibrium compositions in the two phases. Under the same initial conditions, the final microstructures are slightly different, as indicated. This indicates that the cross terms in the PF simulations do not only affect the overall growth rate, but also affect the shape and position of BCC precipitates.

3.2.3. Impact of the presence of a grain boundary.

In experiments it is observed that BCC precipitates are also formed at grain boundaries. To study the impact of grain boundaries on the growth and morphology of the BCC precipitates, a 2D simulation with two BCC precipitates (initial radii of 30 nm and 20 nm) growing at a FCC grain boundary was performed, assuming a system of size 200 nm × 100 nm. The initial concentrations are taken as given in Table 2 for the case Al-CrFeNi (NEQ). Fig. 8 shows the snapshots of microstructures at four different time frames. Fig. 8 (a) shows the initial condition of the simulation with two spherical precipitates at the grain boundary. As the microstructure evolves, the precipitates coalesce together to form an elongated particle, as shown in Fig. 8 (b). Finally, Fig. 8 (c-d) show the fully grown particle that keeps the elongated morphology along the grain boundary. This is mainly mainly due to to the faster diffusion along the grain boundary.

3.2.4. Effect of Al on mobilities and (gradient of) diffusion potentials

The experimental and modeling results both indicate that the average growth rate of the BCC precipitates increases when Al is added to the CrFeNi alloy. This effect could be explained by the influence of Al on the interdiffusion mobilities and the diffusion potential gradients (i.e. the driving forces for diffusion) in the system, which are the 2 key factors that influence the growth rate of the BCC precipitates. To estimate the effect of Al on the mobilities and the diffusion potential gradients,

the simulations of the growth of two BCC precipitates at a grain boundary starting from nonequilibrium initial conditions (cases NEQ in table 2) for the CrFeNi and Al-CrFeNi alloys were considered and the local mobilities and gradients of diffusion potentials of the independent elements, Al, Cr and Fe, were determined from the simulated structures. The results for mobilities and (gradients of) diffusion potentials are non-dimensioned according to Eq. (10) and Eq. (11). Fig. 9a shows the mobilities for CrFeNi at two different time frames, (a) 4207 s and (b) 62254 s, while Fig. 9b shows the mobilities for Al-CrFeNi at time frames of (a) 4312 s and (b) 62284 s. Overall, the mobilities at the grain boundaries are larger than within the matrix for both alloys, since a higher grain boundary diffusion mobility was assumed in the model. The maximum mobility values in Al-CrFeNi are around 11.5 for all elements considered, this is because the grain boundary mobility is increased significantly due to the considerably larger value of Al atomic mobility. While for CrFeNi the maximum mobilities are 0.1 for $\tilde{M}_{CrCr}$, 0.01 for $\tilde{M}_{CrFe}$ and 0.04 for $\tilde{M}_{FeFe}$.

The average values of mobilities for the bulk phases shown in Fig. 9a(b) and Fig. 9b(b) are extracted and are compared in the histogram as shown in Fig. 10. It can be seen that with the addition of Al, the mobilities in both the BCC and FCC phase increase largely. The detailed average values of $\tilde{M}_{CrCr}$, $\tilde{M}_{CrFe}$ and $\tilde{M}_{FeFe}$ for both alloys are listed in Table 5.

Table 5 Comparison of non-dimensional mobilities for bulk phases of the ternary CrFeNi and quaternary Al-CrFeNi alloys

Alloys(phases)	$\boldsymbol{M}_{CrCr}$	$\boldsymbol{M}_{CrFe}$	$\boldsymbol{M}_{FeFe}$
CrFeNi(FCC)	0.0349	-0.0102	0.026
CrFeNi(BCC)	0.000128	-4.2e-5	0.000164
AlCrFeNi(FCC)	0.060926	-0.01698	0.104411
AlCrFeNi (BCC)	0.096717	0.0171549	0.00342

The mobilities in the matrix (FCC phase) is the key factor that influences the growth rate. It is clear that Al addition increases the diagonal elements $\tilde{M}_{CrCr}$ and $\tilde{M}_{FeFe}$ of the diffusion matrix contributing to the faster growth. Moreover, it was shown (Section 3.2.2) that the cross terms have a

more extensive effect on the growth rate in the quaternary alloy than on the ternary system. This can also be understood based on the values listed in Table 5 for the mobility $\tilde{M}$CrFe, which is larger in absolute value for the quaternary system than for the ternary. Moreover, for the ternary system there is only one independent cross term, while for the quaternary system, there are three (with corresponding nondimensional mobility values $\tilde{M}$CrFe: -0.01698, $\tilde{M}$AlFe: -0.03336, and $\tilde{M}$CrAl: -0.01556).

The gradient of the diffusion potential $\tilde{\mu}_j = \frac{\partial F}{\partial x_i}$ is the driving force for the movement of the atoms in the material. Fig. 11a shows the diffusion potentials for CrFeNi (nonequilibrium initial condition) with two BCC precipitates in the system at time frames of (a) 4207 s and (b) 62254 s. Fig. 11b shows the diffusion potentials for Al-CrFeNi (nonequilibrium initial condition) with the same initial geometry in the system at time frames of (a) 4312 s and (b) 62284 s. The scale bar considers the whole data range. Results show that $\tilde{\mu}_{Cr} and \tilde{\mu}_{Fe}$ in CrFeNi are within the range 2.4~2.5 and 1.0~1.1, respectively at simulation time 62254s, and that $\tilde{\mu}_{Cr} and \tilde{\mu}_{Fe}$ in Al-CrFeNi are within the range 2.68~2.85 and 1.48~1.54 at 62284s, respectively. The data in the contours are larger in Al-CrFeNi, which indicates that the diffusion potentials of Cr and Fe are larger for Al-CrFeNi. The diffusion potential for Al also presents a substantial absolute value yet (negative value around -11). It is clear that the addition of Al in the CrFeNi alloys results in an overall increase of the diffusion potentials for Cr and Fe.

To estimate the influence of Al on the driving force, the corresponding gradient of the diffusion potential for both alloys is also plotted and shown in Fig. 12a and Fig. 12b. The scale bar considers the whole data range for Fig. 12a (a) and Fig. 12b (a), while the scale bar for Fig. 12a (b) and Fig. 12b (b) keep the same range. Overall, the values of $\nabla \tilde{\mu}_i$ are decreasing in time since the system is evolving towards the equilibrium state. Results also show that the values are larger around the precipitate / matrix interface. The red color in the contour represents the maximum value for the gradient of diffusion potential. Fig. 12a (a), Fig. 12b (a) show the maximum values of $\nabla \tilde{\mu}_{Cr}$ and $\nabla \tilde{\mu}_{Fe}$ are 0.017 and 0.011, respectively in CrFeNi, which is slightly smaller than the corresponding values (∇

$\nabla \tilde{\mu}_{Cr}$:0.02, $\nabla \tilde{\mu}_{Fe}$:0.03) in Al-CrFeNi. The red area is also wider in Al-CrFeNi, which reveals that with addition of Al, there is a decrease in the gradients of the diffusion potentials for Cr and Fe, contributing to the faster growth of the precipitates. Mehta[56] et al, also shows that the Al will influence the overall mixing enthalpy (ΔH_{mix}) and also the Gibbs energy (ΔG_{mix}) and thus influence the driving forces. This is consistent with our findings on the effect of Al on the thermodynamic driving forces for diffusion $\nabla \tilde{\mu}_{k}$.

3.3. Discussion

The compositions of the alloys were specifically chosen based on thermodynamic calculations to produce a system featuring both FCC and BCC phases at high temperature. Experimental results confirm the precipitation of BCC phase in both the quaternary Al-CrFeNi and ternary CrFeNi alloy investigated, which is in agreement with the predictions from thermodynamic calculations. The Sigma phase was not observed in the experiments as usually presented when alloys enriched with Cr and Fe after aging for a long-time at 700 °C. Adding Al to the ternary CrFeNi system has the main effect of stabilizing the BCC structure. Indeed, the effect of Al as a potent stabilizer of BCC structure in HEAs is well documented in literature [17,18], and it is confirmed in the present paper. The equilibrium volume fraction of BCC at 700°C increases from 15 vol.% to 24 vol.% following the addition of 5 at.% Al to the CrFeNi system.

Aside from the effect on the thermodynamics of the systems, the addition of 5 at.% Al increases the precipitation and growth rate of the BCC particles, as shown in Fig. 3. The quaternary Al-CrFeNi alloy reaches the thermodynamic equilibrium (24 vol.%) predicted by thermodynamic calculations after approximately 200 hours of aging. On the other hand, the growth rate of BCC in the ternary alloy is slower and still far from the calculated equilibrium (15 vol.%) even after 11 days. The effect of Al addition on the growth rate of the BCC phase was already observed experimentally by Shun et al.[26]. and Lin et al.[27] in HEAs containing Al. In the present work, the experimental findings are rationalized on the base of PF simulations that highlight the fundamental mechanism driving the

faster BCC growth in presence of Al. Indeed, PF simulations reveal that interdiffusion mobility and the driving force for the interdiffusion, which are the main factors affecting the growth rate of BCC particles, increase with the addition of Al, as shown in Fig. 10 and Fig. 12, respectively. Thus, these combined factors contribute to the rapid growth of the BCC precipitates in Al-CrFeNi alloy compared with Al free CrFeNi alloy as outlined by the experimental findings.

Moreover, the simulations indicate that the resulting microstructure evolution for BCC and FCC are different under the same initial conditions depending on whether the cross terms in the diffusion equations are taken into account, as quantified and discussed in section 3.2.2. The cross interactions between elements, i.e., the gradient in diffusion potential of one element can drive diffusion of another element, thus affect the growth rate of BCC precipitates and, moreover, influences the BCC precipitate shape and distribution in the microstructure, clearly illustrating the importance of considering the full complexity of multicomponent models to fully understand the interdiffusion behavior and microstructure formation in high and medium entropy alloys.

3.3.1. Phase Morphology

In addition to the general kinetics, PF simulations greatly contribute to the understanding of the observed morphology of BCC precipitates in both ternary CrFeNi and quaternary Al-CrFeNi alloys. Experimental results show that grain boundaries (GB) are the preferred sites for BCC precipitation for shorter holding times at 700°C. This precipitation behaviour, which is often observed in the literature, can be further rationalized based on the PF simulation results. In both studied alloys, the gradient of the diffusion potential is larger at the GBs, revealing that GBs are preferential sites of secondary phase precipitation. The PF model provides a visual impression of the microstructure evolution during a phase transition, which can be of great help in the design of multicomponent alloys. It is however still a limitation of the method that simulations quickly become computationally challenging when considering larger domains. In order to model the rod-like or lenticular intra-granular precipitation of BCC_A2 phase shown in the quaternary Al-CrFeNi alloy, the interface anisotropy, elastic effects and other structure-related parameters, etc, should also be considered. Further research and model

development and implementation is thus required. Indeed, this peculiar precipitation morphology is also observed elsewhere for AlxCoCrFeNi[26,57], in which a Kurdjumov–Sachs (K–S) relationship is identified between the rod-like B2 precipitate and the matrix, thus indicating a full coherency between those particles and the FCC matrix phase.

3.4. Conclusions

Based on thermodynamic calculations, it was decided to study the effect of addition of 5 at.% Al to the ternary CrFeNi equimolar system on the FCC to BCC phase transformation. The experimental findings show a clearly different time evolution of the BCC phase fraction for the cases with and without the 5 at% Al, which increased substantially faster in the Al-CrFeNi alloy than in the ternary CrFeNi alloy. This difference in growth kinetics is explained based on multicomponent PF simulation results obtained for the same alloy compositions. The main findings are:

- In the 5at%Al - CrFeNi alloy, the BCC phase fraction increases rapidly and reaches thermodynamic equilibrium already after approximately 200 hours of aging at 700 °C. Firstly, the precipitation is confined to the grain boundary, which is soon followed by intergranular precipitation of lenticular-shaped particles for longer holding at 700 °C.
- In CrFeNi, the evolution of BCC phase fraction presents more sluggish kinetics. The system does not reach thermodynamic equilibrium even after 270 hours of aging. In this system, BCC precipitation is mainly idiomorphic and confined to the grain boundary.
- A small amount of Al addition into a CrFeNi equal atomic ternary alloy considerably increases the interdiffusion mobilities. The gradient of diffusion potential $\nabla \tilde{\mu}_i$ (i=Cr, Fe), which represents the fundamental driving force of the phase transformation and the interdiffusion mobilities in the FCC phase are also both increased. These factors are the key for understanding the higher growth rate of BCC precipitates in the Al-added CrFeNi alloy compared with the Al-free CrFeNi alloy.

- It was also verified that the cross terms in the PF model affect the growth rate of BCC precipitates and influence the evolution of the microstructure, which confirms the necessity of developing advanced multicomponent models.

The findings in this paper contribute to a better understanding of the complex interdiffusion behavior in high and medium entropy alloys. This PF simulation can be applied to any system if the thermodynamic and kinetic database are available and will foster the design of multicomponent alloys and predict the phase growth behavior before the experimental studies are performed.

Acknowledgements

The research was partly funded by the Walloon Region under the agreement No. 1610154-EntroTough in the context of the 2016 WallInnov call. The simulation work was supported by the European Research Council (ERC) under the European Union's Horizon 2020 research and innovation program (INTERDIFFUSION, grant agreement no. 714754). The computational resources and services used in this work were provided by the VSC (Flemish Supercomputer Center), funded by the Research Foundation - Flanders (FWO) and the Flemish Government - department EWI.

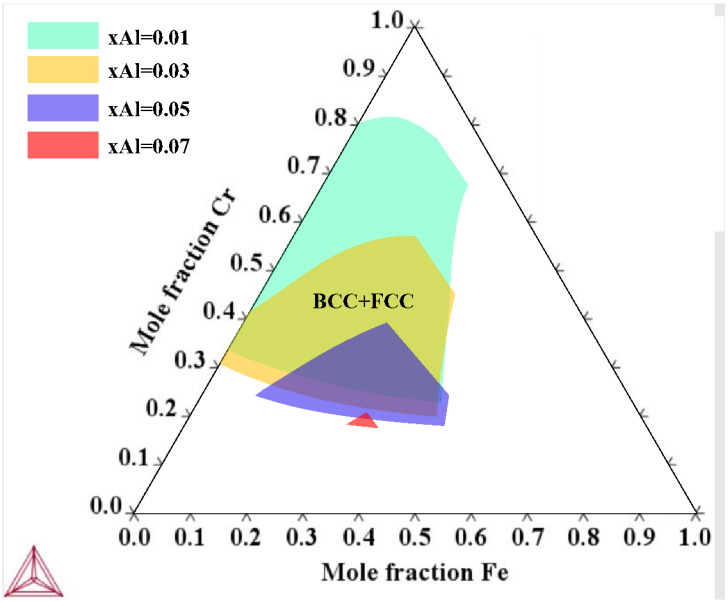

Fig. 1 BCC/FCC two-phase region in the ternary sections of the AlCrNiFe phase diagram for fixed amounts of Al

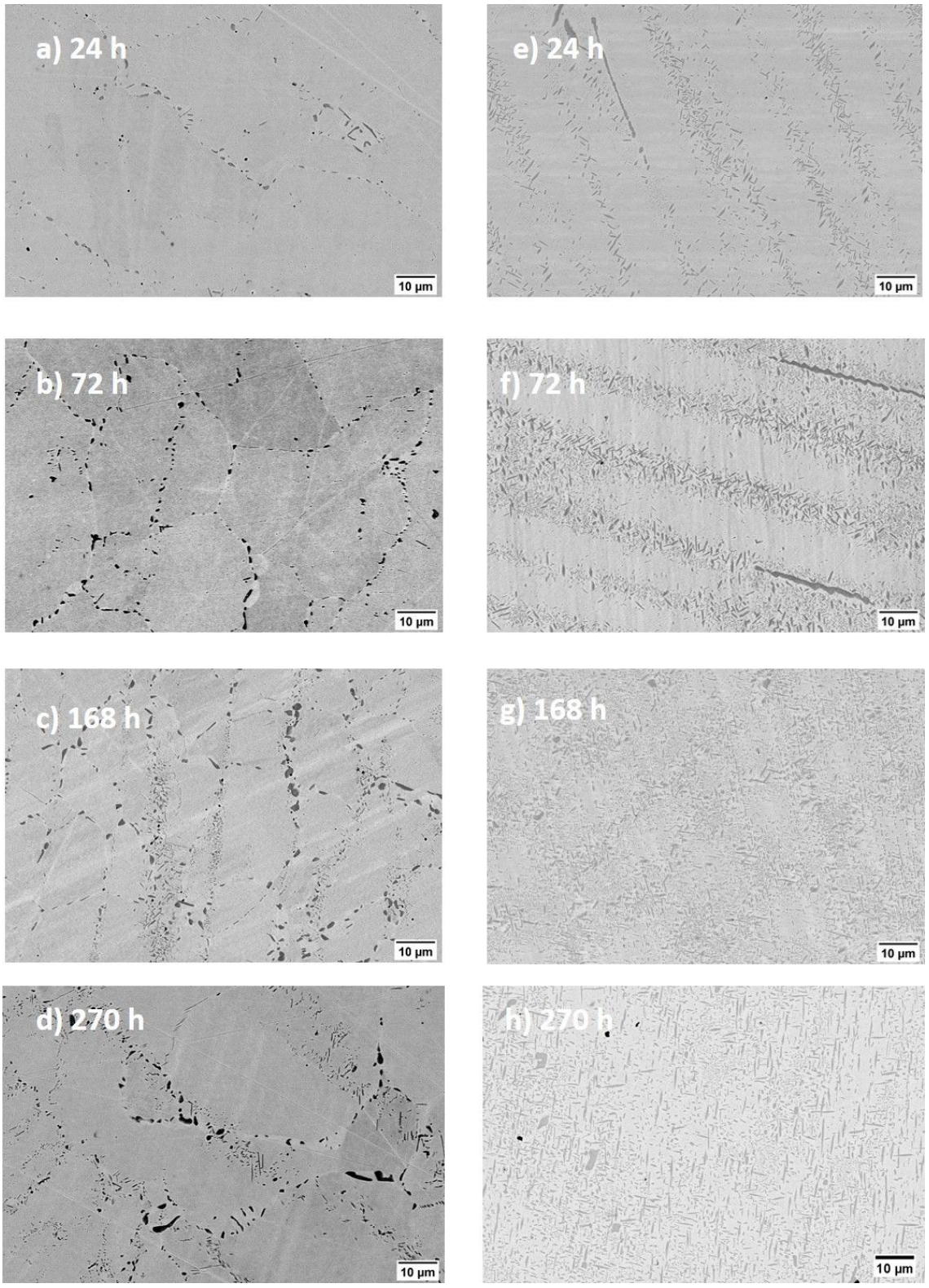

Fig. 2 SEM-BSE micrographs showing the evolution of microstructure at 0h,, 72h, 168h and 270h during isothermal aging at 700°C for (a,b,c,d) ternary CrFeNi and (e,f,g,h) quaternary Al-CrFeNi systems.

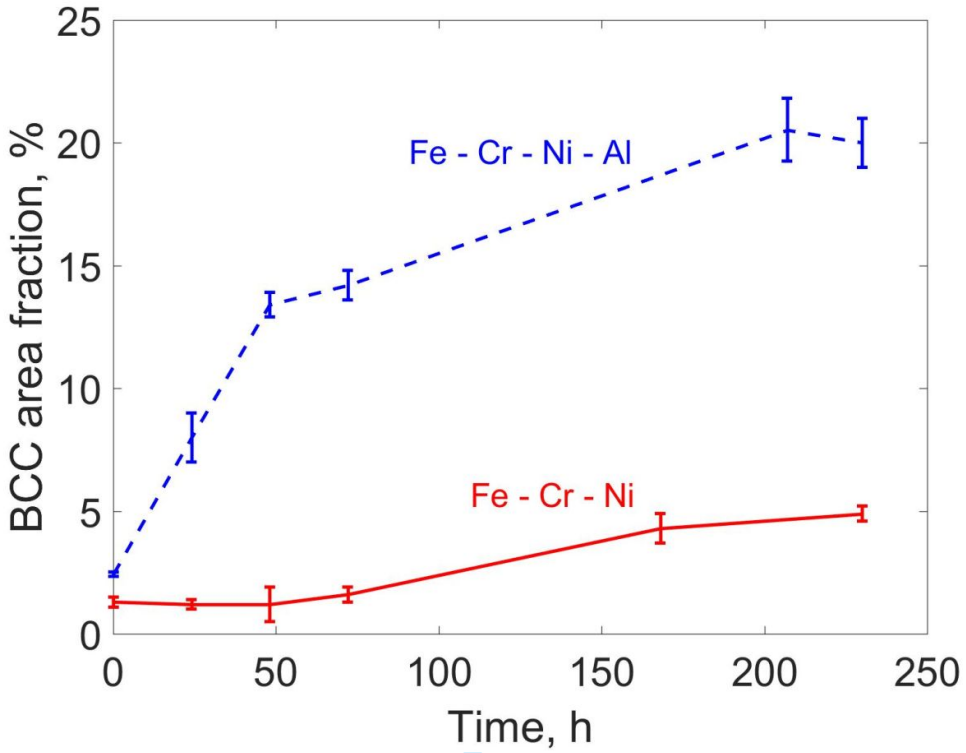

Fig. 3 BCC area fraction evolution during isothermal aging at 700°C for quaternary Al-CrFeNi (blue, dotted line) and ternary CrFeNi (red, solid line) alloys.

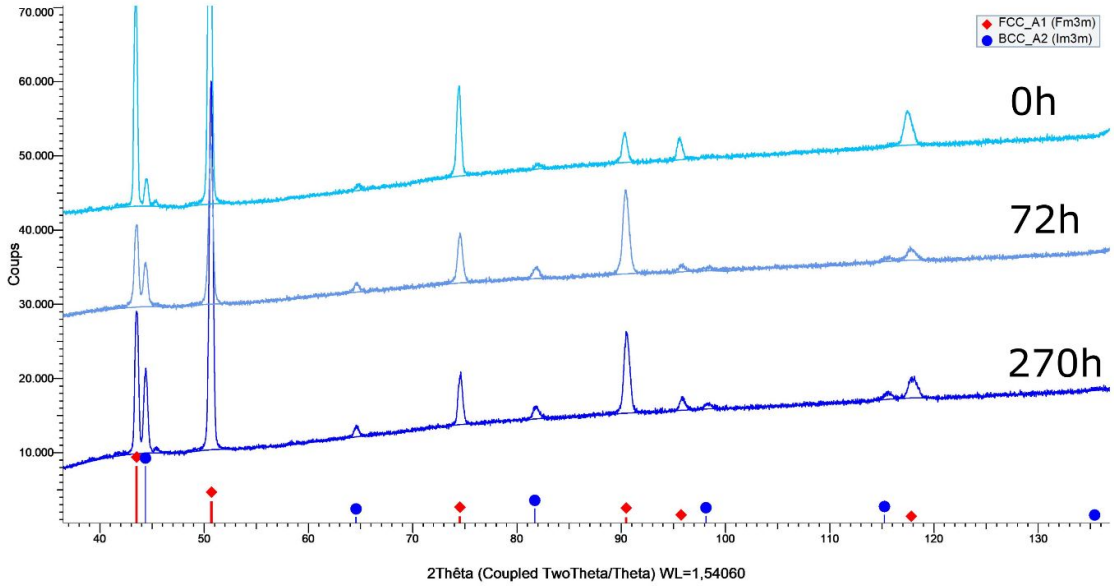

Fig. 4 X-Ray diffraction spectra for 0h, 72h and 270h holding at 700°C for Al-CrFeNi alloy showing the presence of a disordered FCC-type (space group Fm3m, highlighted in red) and BCC-type (space group Im3m, highlighted in blue) phase. The intensity of peaks related to BCC phase is increasing for longer holding times at 700°C, which agrees with the increment of volume fraction of the secondary phase.

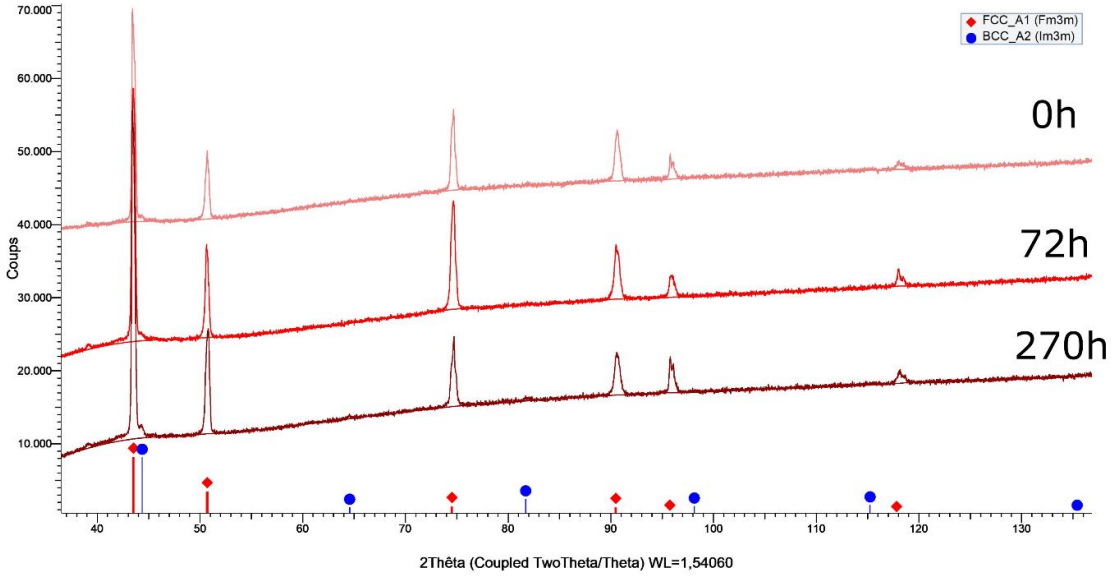

Fig. 5 X-Ray diffraction spectra for 0h, 72h and 270h holding at 700°C for Al-free ternary CrFeNi alloy showing the predominance of FCC-type phase in the alloy. A low-intensity peak corresponding to disordered BCC phase (2Theta = 44°) is being detected only after 270h holding at 700°C.

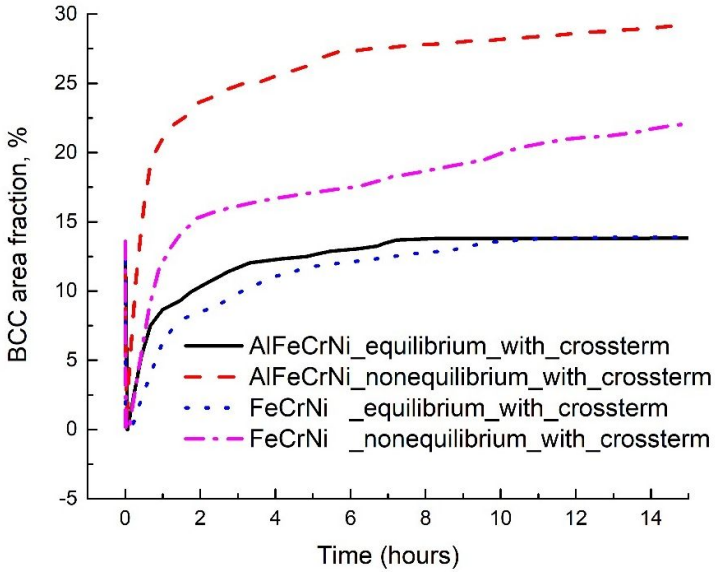

Fig. 6 Comparison of the evolution of BCC precipitate area fraction with time in the phase-field simulations for CrFeNi and Al-CrFeNi for an initial structure having the equilibium composition in both the FCC and BCC phase (indicated with 'equilibrium' in the legend) (case EQ in table 2) and an initial structure with FCC composition deviating from the equilibrium (indicated with 'non-equilibrium' in the legend)(case NEQ in table).

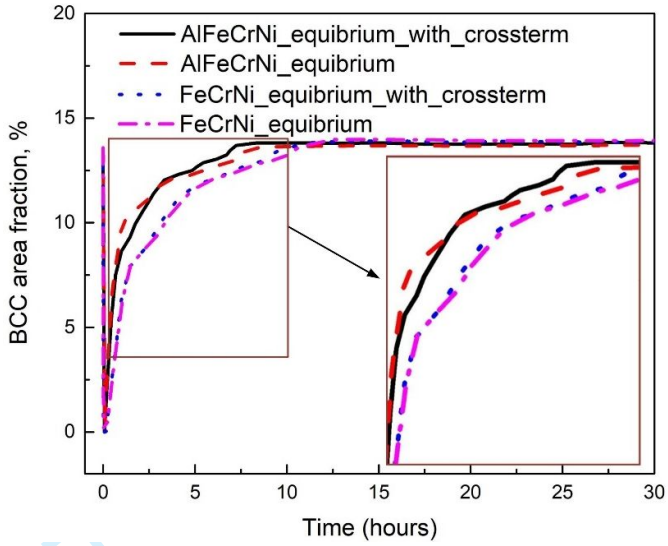

Fig. 7a Comparison of the growth area fraction with time of BCC precipitates in simulations (with or without crossterm in the PF calculation) for different alloy systems under same initial conditions.

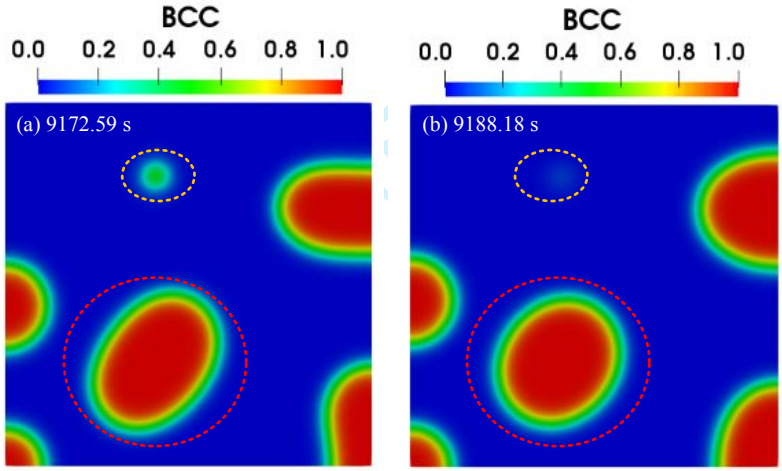

Fig. 7b PF simulation images representing the microstructure with BCC precipitates in FCC matrix for the Al-CrFeNi alloy obtained using the model (a) with crossterms and (b) without crossterms, and at similar simulation times, namely (a) 9172.59s and (b) 9188.18s. The initial structure with equilibrium BCC and FCC composition was used.

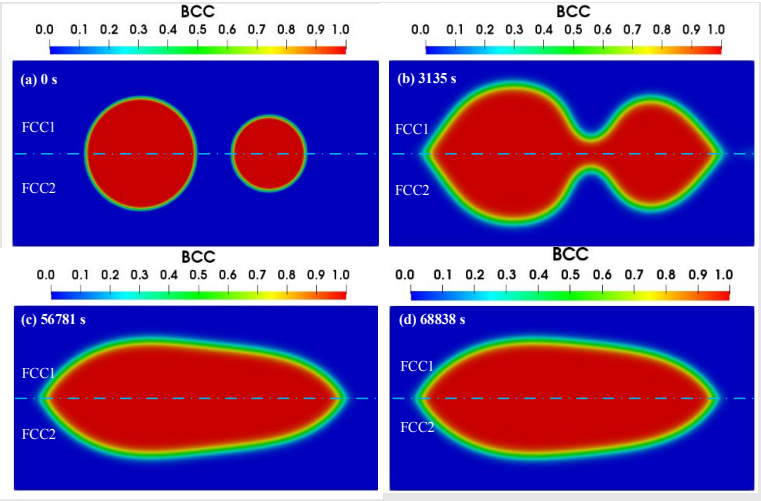

Fig. 8 Images of the PF simulation of 2 BCC precipitates growing at an FCC grain boundary in Al-CrFeNi obtained at time frames (a) 0 s (b) 3135 s (c) 56784s (d) 68838 s. The initial microstructure with non-equilibrium composition in the FCC phase (NEQ) is considered.

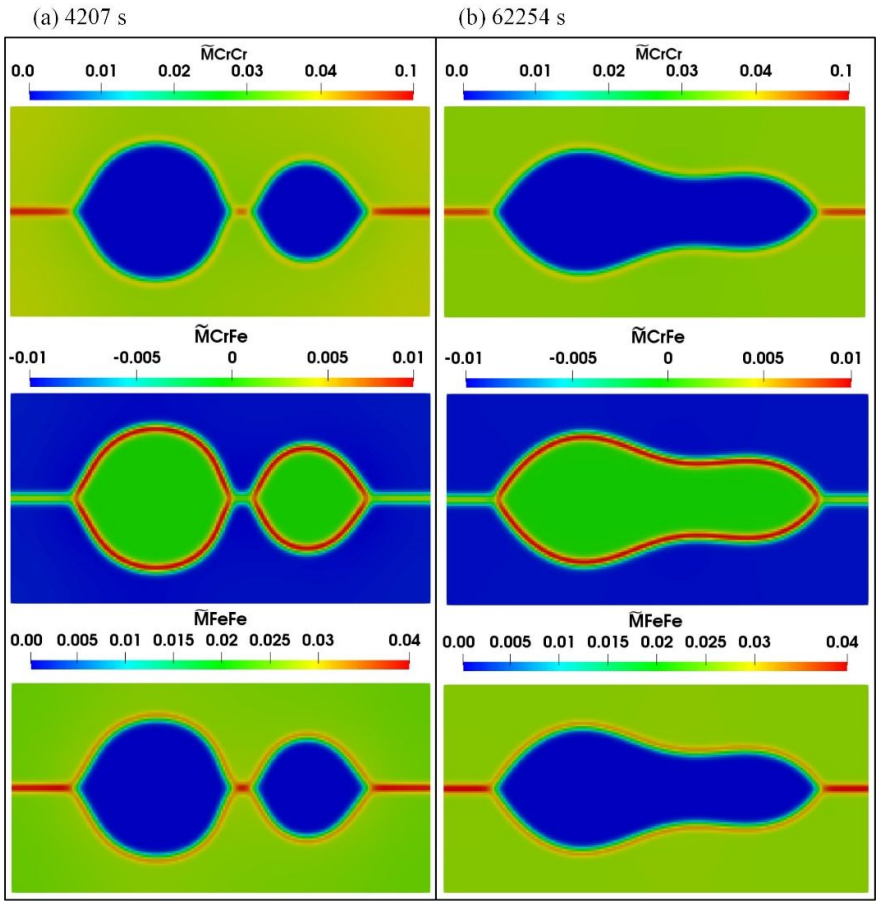

Fig. 9a Local mobility values as obtained from the PF simulations for CrFeNi (with initial nonequilibrium composition in FCC phase) at times (a) 4207 s (b) 62254 s.

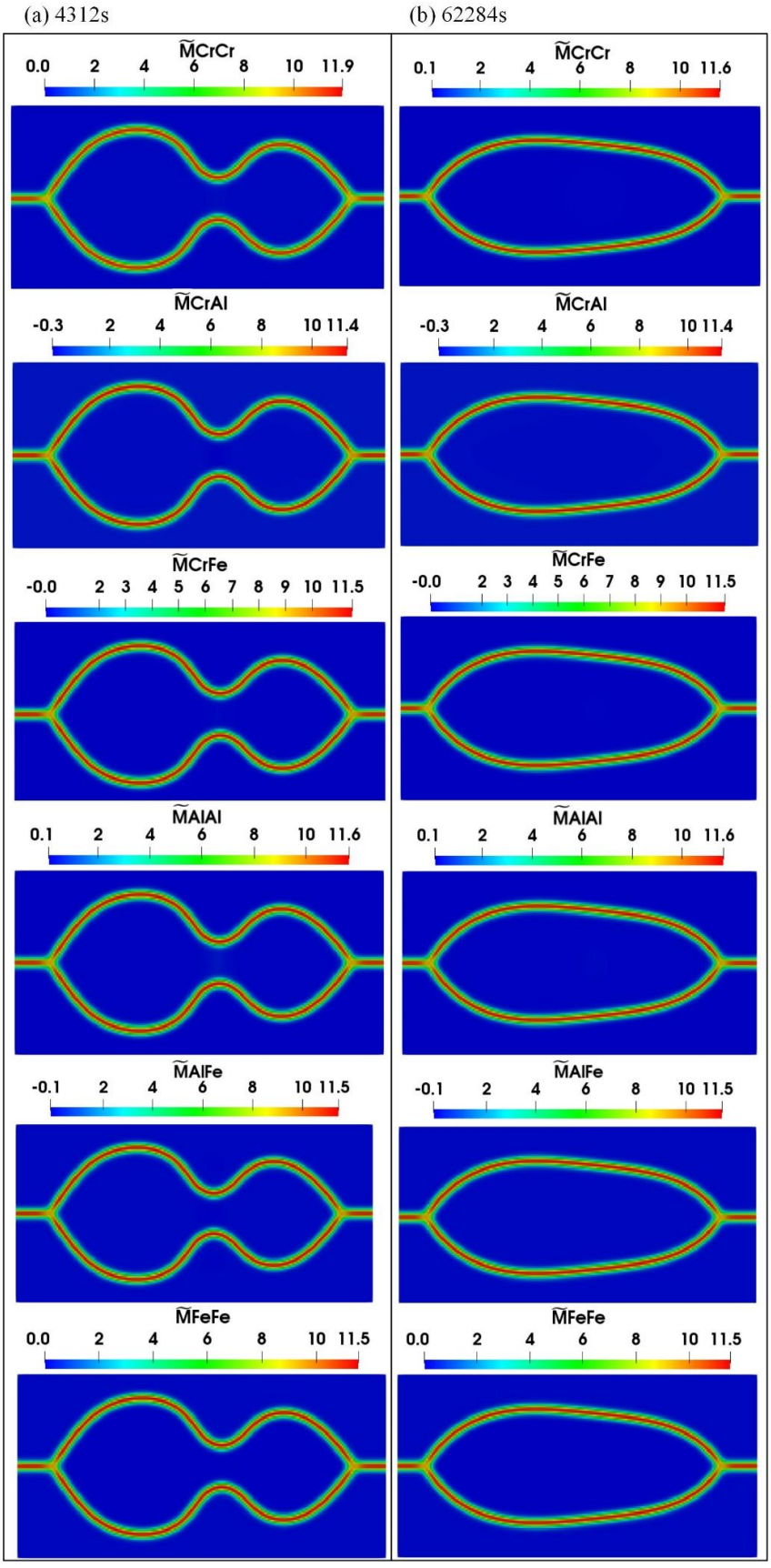
(a) 4312s
(b) 62284s
$\widetilde{M}$CrCr
0.0 2 4 6 8 10 11.9
0.1 2 4 6 8 10 11.6
$\widetilde{M}$CrAl
-0.3 2 4 6 8 10 11.4
$\widetilde{M}$CrFe
-0.0 2 3 4 5 6 7 8 9 10 11.5
$\widetilde{M}$AlAl
0.1 2 4 6 8 10 11.6
$\widetilde{M}$AlFe
-0.1 2 4 6 8 10 11.5
$\widetilde{M}$FeFe
0.0 2 4 6 8 10 11.5

Fig. 9b Local diffusion mobility values as obtained from PF simulations for Al-CrFeNi (with initial nonequilibrium composition) at time frames (a) 4312 s (b) 62284 s

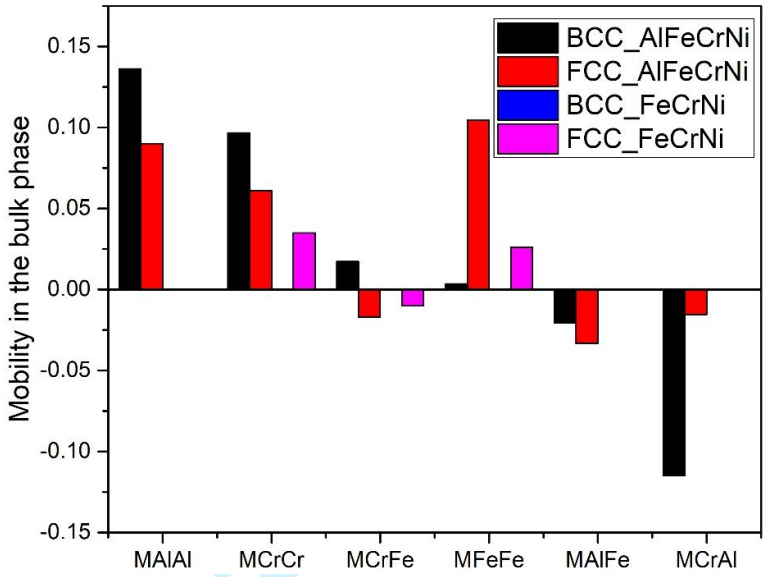

Fig. 10 Average dimensionless mobilities in BCC/FCC for Al-CrFeNi (nonequilibrium) at time frames (a) 62284 s and CrFeNi (nonequilibrium) (b) 62254 s

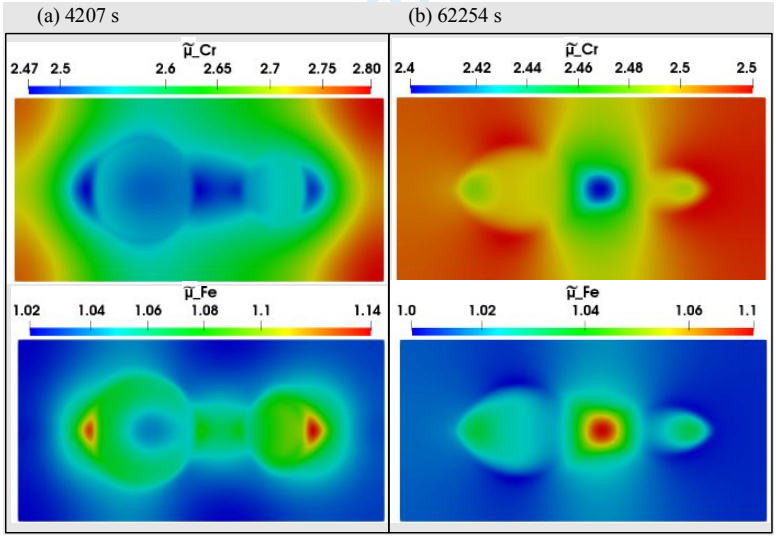

Fig. 11a Local values of the diffusion potentials as obtained from PF simulations for CrFeNi (case NEQ in table 2) at time frame (a) 4207 s and (b) 62254 s

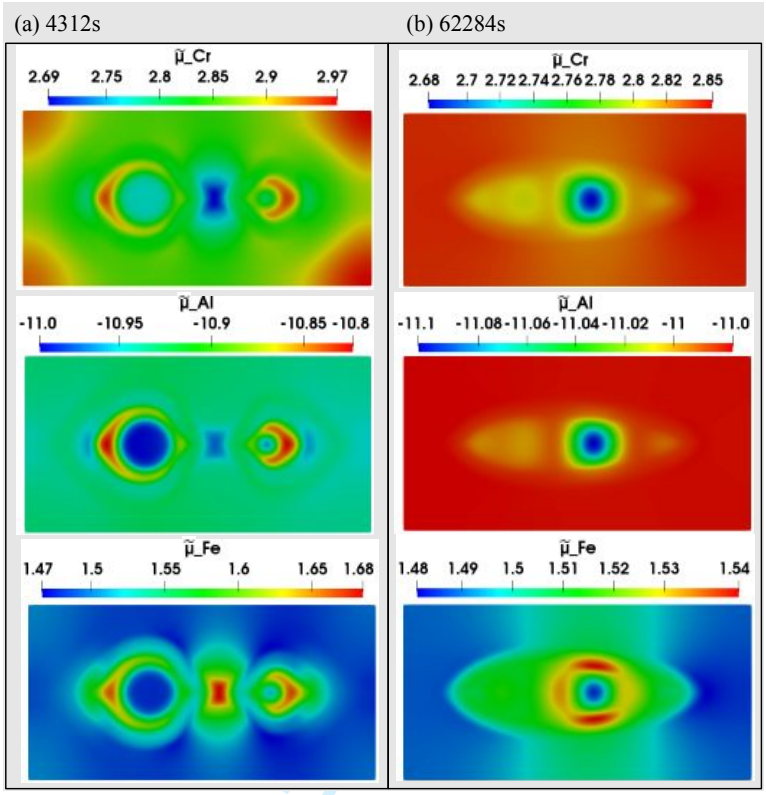

Fig. 11b Local values of the diffusion potentials from PF simulations for Al-CrFeNi (case NEQ in Table 2) at time frame(a) 4312 s (b) 62284 s

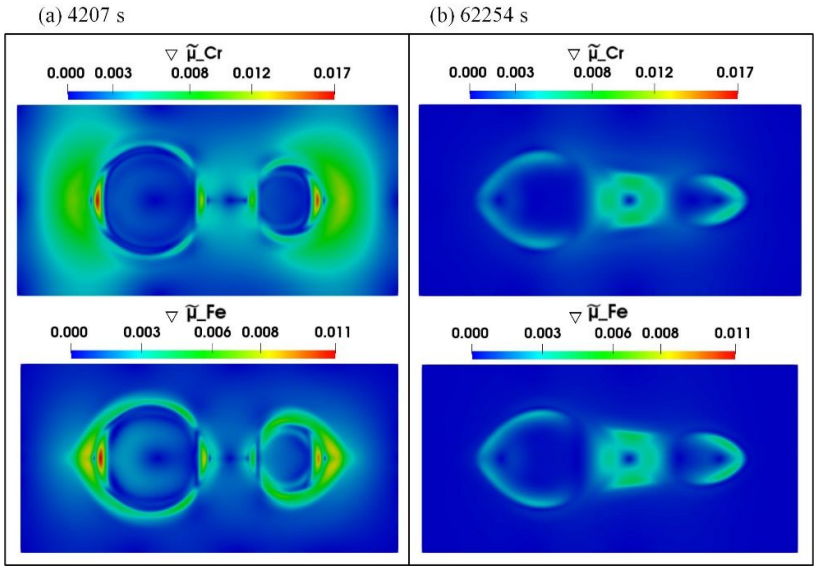

Fig. 12a Local values of the gradient of diffusion potentials obtained from PF simulations for CrFeNi (case NEQ in Table 2) at time frame(a) 4207 s (b) 62254 s

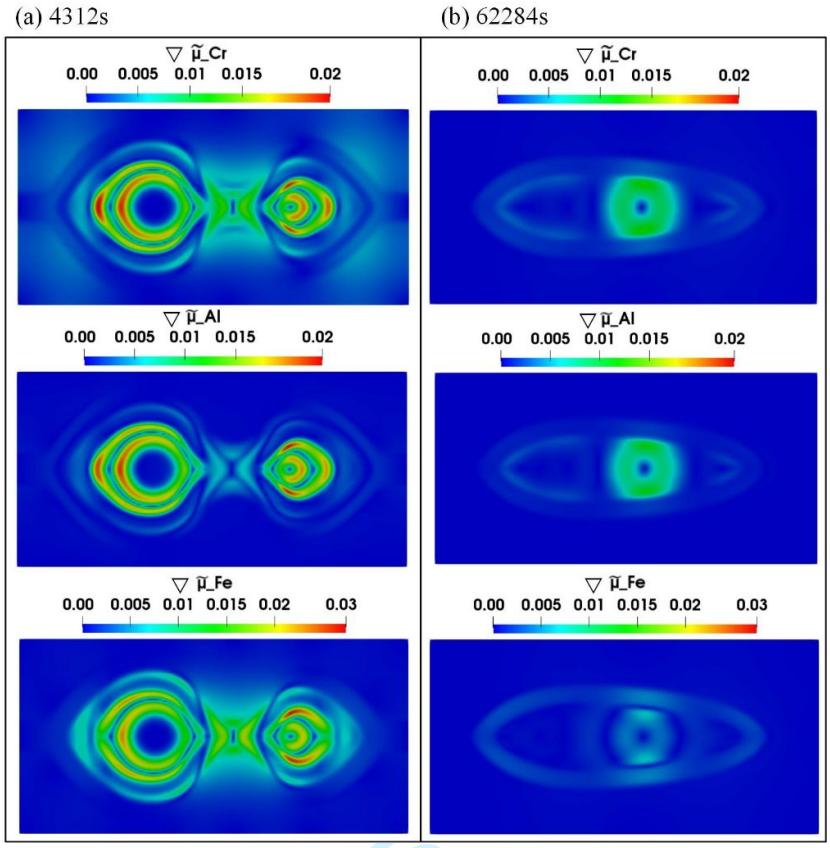

Fig. 12b Local values of the gradient diffusion potentials obtained from PF simulations for Al-CrFeNi (case NEQ in Table 2) at time frame(a) 4312 s (b) 62284 s

4. References

1. E.P. George, D. Raabe, and R.O. Ritchie, High-entropy alloys, *Nat. Rev. Mater.*, 2019, **4**(8), p 515–534
2. D.B. Miracle and O.N. Senkov, A critical review of high entropy alloys and related concepts, *Acta Mater.*, 2017, **122**, p 448–511
3. O.N. Senkov, D.B. Miracle, K.J. Chaput, and J.P. Couzinie, Development and exploration of refractory high entropy alloys—A review, *J. Mater. Res.*, 2018, **33**(19), p 3092–3128
4. E.J. Pickering and N.G. Jones, High-entropy alloys: a critical assessment of their founding principles and future prospects, *Int. Mater. Rev.*, 2016, **61**(3), p 183–202
5. G. Laplanche, A. Kostka, O.M. Horst, G. Eggeler, and E.P. George, Microstructure evolution and critical stress for twinning in the CrMnFeCoNi high-entropy alloy, *Acta Mater.*, 2016, **118**, p 152–163

6. G. Singh, H. Chan, A. Baskin, E. Gelman, N. Repnin, P. Král, and R. Klajn, Self-assembly of magnetite nanocubes into helical superstructures, *N. Y. Sci. J.*, 2014, **345**(6201), p 1149–1153
7. J. Miao, C.E. Slone, T.M. Smith, C. Niu, H. Bei, M. Ghazisaeidi, G.M. Pharr, and M.J. Mills, The evolution of the deformation substructure in a Ni-Co-Cr equiatomic solid solution alloy, *Acta Mater.*, 2017, **132**, p 35–48
8. G. Laplanche, A. Kostka, C. Reinhart, J. Hunfeld, G. Eggeler, and E.P. George, Reasons for the superior mechanical properties of medium-entropy CrCoNi compared to high-entropy CrMnFeCoNi, *Acta Mater.*, 2017, **128**, p 292–303
9. B. Gludovatz, A. Hohenwarter, K.V.S. Thurston, H. Bei, Z. Wu, E.P. George, and R.O. Ritchie, Exceptional damage-tolerance of a medium-entropy alloy CrCoNi at cryogenic temperatures, *Nat. Commun.*, 2016, **7**, p 10602
10. D. Choudhuri, M. Komarasamy, V. Ageh, and R.S. Mishra, Investigation of plastic deformation modes in Al0.1CoCrFeNi high entropy alloy, *Mater. Chem. Phys.*, 2018, **217**, p 308–314
11. D. Choudhuri, S. Shukla, B. Gwalani, R. Banerjee, and R.S. Mishra, Deformation induced intermediate metastable lattice structures facilitate ordered B2 nucleation in a fcc-based high entropy alloy, *Mater. Res. Lett.*, 2019, **7**(1), p 40–46
12. S. Gangireddy, B. Gwalani, K. Liu, R. Banerjee, and R.S. Mishra, Microstructures with extraordinary dynamic work hardening and strain rate sensitivity in Al0.3CoCrFeNi high entropy alloy, *Mater. Sci. Eng. A .*, 2018, **734**, p 42–50
13. S. Gangireddy, B. Gwalani, V. Soni, R. Banerjee, and R.S. Mishra, Contrasting mechanical behavior in precipitation hardenable AlXCoCrFeNi high entropy alloy microstructures: Single phase FCC vs. dual phase FCC-BCC, *Mater. Sci. Eng. A .*, 2019, **739**, p 158–166
14. S. Gangireddy, D. Whitaker, and R.S. Mishra, Significant Contribution to Strength Enhancement from Deformation Twins in Thermomechanically Processed Al0.1CoCrFeNi Microstructures, *J. of Materi Eng and Perform*, 2019, **28**(3), p 1661–1667
15. D. Li and Y. Zhang, The ultrahigh charpy impact toughness of forged AlxCoCrFeNi high entropy alloys at room and cryogenic temperatures, *Intermetallics*, 2016, **70**, p 24–28
16. S.Q. Xia, M.C. Gao, and Y. Zhang, Abnormal temperature dependence of impact toughness in Al CoCrFeNi system high entropy alloys, *Mater. Chem. Phys.*, 2018, **210**, p 213–221
17. J.Y. He, W.H. Liu, H. Wang, Y. Wu, X.J. Liu, T.G. Nieh, and Z.P. Lu, Effects of Al addition on structural evolution and tensile properties of the FeCoNiCrMn high-entropy alloy system, *Acta Mater.*, 2014, **62**, p 105–113
18. C. Zhang, F. Zhang, H. Diao, M.C. Gao, Z. Tang, J.D. Poplawsky, and P.K. Liaw, Understanding phase stability of Al-Co-Cr-Fe-Ni high entropy alloys, *Mater. Des.*, 2016, **109**, p 425–433

19. H. Yang, J. Li, T. Guo, W.Y. Wang, H. Kou, and J. Wang, Fully Recrystallized Al0.5CoCrFeNi High-Entropy Alloy Strengthened by Nanoscale Precipitates, *Met. Mater. Int.*, 2019, **25**(5), p 1145–1150
20. Q. Li, T.W. Zhang, J.W. Qiao, S.G. Ma, D. Zhao, P. Lu, and Z.H. Wang, Mechanical properties and deformation behavior of dual-phase Al0.6CoCrFeNi high-entropy alloys with heterogeneous structure at room and cryogenic temperatures, *J. Alloy Compd.*, 2020, **816**, p 152663
21. Y.Y. Du, Y.P. Lu, T.J. Li, T.M. Wang, and G.L. Zhang, Effect of aluminium content of Al x CrFe 1·5 Ni 0·5 multiprincipal alloys on microstructure and alloy hardness, *Mater. Res. Innov.*, 2011, **15**(2), p 107–110
22. W.R. Wang, W.L. Wang, and J.W. Yeh, Phases, microstructure and mechanical properties of AlxCoCrFeNi high-entropy alloys at elevated temperatures, *J. Alloy Compd.*, 2014, **589**, p 143–152
23. J. Zeng, C. Wu, H. Peng, Y. Liu, J. Wang, and X. Su, Microstructure and microhardness of as-cast and 800 °C annealed Al x Cr 0.2 Fe 0.2 Ni 0.6-x and Al 0.2 Cr 0.2 Fe y Ni 0.6-y alloys, *Vacuum*, 2018, **152**, p 214–221
24. T. Yang, S. Xia, S. Liu, C. Wang, S. Liu, Y. Zhang, J. Xue, S. Yan, and Y. Wang, Effects of AL addition on microstructure and mechanical properties of Al CoCrFeNi High-entropy alloy, *Mater. Sci. Eng. A* ., 2015, **648**, p 15–22
25. W.R. Wang, W.L. Wang, S.C. Wang, Y.C. Tsai, C.H. Lai, and J.W. Yeh, Effects of Al addition on the microstructure and mechanical property of AlxCoCrFeNi high-entropy alloys, *Intermetallics*, 2012, **26**, p 44–51
26. T.T. Shun and Y.C. Du, Microstructure and tensile behaviors of FCC Al0.3CoCrFeNi high entropy alloy, *J. Alloy Compd.*, 2009, **479**(1-2), p 157–160
27. C.M. Lin and H.L. Tsai, Evolution of microstructure, hardness, and corrosion properties of high-entropy Al0.5CoCrFeNi alloy, *Intermetallics*, 2011, **19**(3), p 288–294
28. Z. Tang, M.C. Gao, H. Diao, T. Yang, J. Liu, T. Zuo, Y. Zhang, Z. Lu, Y. Cheng, Y. Zhang, K.A. Dahmen, P.K. Liaw, and T. Egami, Aluminum Alloying Effects on Lattice Types, Microstructures, and Mechanical Behavior of High-Entropy Alloys Systems, *JOM*, 2013, **65**(12), p 1848–1858
29. C. Zhang, F. Zhang, S. Chen, and W. Cao, Computational Thermodynamics Aided High-Entropy Alloy Design, *JOM*, 2012, **64**(7), p 839–845
30. A.H. Tkaczyk, A. Bartl, A. Amato, V. Lapkovskis, and M. Petranikova, Sustainability evaluation of essential critical raw materials: cobalt, niobium, tungsten and rare earth elements, *J. Phys. D: Appl. Phys.*, 2018, **51**(20), p 203001

31. X. Chen, Y. Sui, J. Qi, Y. He, F. Wei, Q. Meng, and Z. Sun, Microstructure of Al 1.3 CrFeNi eutectic high entropy alloy and oxidation behavior at 1000 °C, *J. Mater. Res.*, 2017, **32**(11), p 2109–2116
32. X. Chen, J.Q. Qi, Y.W. Sui, Y.Z. He, F.X. Wei, Q.K. Meng, and Z. Sun, Effects of aluminum on microstructure and compressive properties of Al-Cr-Fe-Ni eutectic multi-component alloys, *Mater. Sci. Eng. A* ., 2017, **681**, p 25–31
33. Y. Dong, X. Gao, Y. Lu, T. Wang, and T. Li, A multi-component AlCrFe2Ni2 alloy with excellent mechanical properties, *Mater. Lett.*, 2016, **169**, p 62–64
34. F. Tian, L. Delczeg, N. Chen, L.K. Varga, J. Shen, and L. Vitos, Structural stability of NiCoFeCrAl x high-entropy alloy from ab initio theory, *Phys. Rev. B*, 2013, **88**(8)
35. E. Eshed, S. Abd El Majid, M. Bamberger, and S. Osovski, TEM and High Resolution TEM Investigation of Phase Formation in High Entropy Alloy AlCrFe2Ni2, *Frontiers in Materials*, 2020, **7**
36. L.Q. Chen, Phase-Field Models for Microstructure Evolution, *Annu. Rev. Mater. Res.*, 2002, **32**(1), p 113–140
37. N. Moelans, B. Blanpain, and P. Wollants, An introduction to phase-field modeling of microstructure evolution, *Calphad*, 2008, **32**, p 268–294
38. Y. Li, S. Hu, X. Sun, and M. Stan, A review: applications of the phase field method in predicting microstructure and property evolution of irradiated nuclear materials, *npj Comput Mater*, 2017, **3**(1), p 11
39. J. Zhou, J. Odqvist, L. Höglund, M. Thuvander, T. Barkar, and P. Hedström, Initial clustering – a key factor for phase separation kinetics in Fe–Cr-based alloys, *Scr. Mater.*, 2014, **75**, p 62–65
40. G. Mi, L. Xiong, C. Wang, P. Jiang, and G. Zhu, Two-dimensional phase-field simulations of competitive dendritic growth during laser welding, *Mater. Des.*, 2019, **181**, p 107980
41. B. Nestler and A. A. Wheeler, Phase-field modeling of multi-phase solidification, *Comput. Phys. Commun.*, 2002, p 230–233
42. Q. Chen, N. Ma, K. Wu, and Y. Wang, Quantitative phase field modeling of diffusion-controlled precipitate growth and dissolution in Ti–Al–V, *Scr. Mater.*, 2004, **50**(4), p 471–476
43. T. Naseri, D. Larouche, R. Martinez, F. Breton, and D. Massinon, Analytical Modeling of the Mixed-Mode Growth and Dissolution of Precipitates in a Finite System, *Metals*, 2019, **9**(8), p 889
44. L. Hou, N. Moelans, J. Derakhshandeh, I. de Wolf, and E. Beyne, Study of the effect of Sn grain boundaries on IMC morphology in solid state inter-diffusion soldering, *Sci. Rep.*, 2019, **9**(1), p 14862
45. J.L. Li, Z. Li, Q. Wang, C. Dong, and P.K. Liaw, Phase-field simulation of coherent BCC/B2 microstructures in high entropy alloys, *Acta Mater.*, 2020, **197**, p 10–19

46. A. Malik, J. Odqvist, L. Höglund, S. Hertzman, and J. Ågren, Phase-Field Modeling of Sigma-Phase Precipitation in 25Cr7Ni4Mo Duplex Stainless Steel, *Metall and Mat Trans A*, 2017, **48**(10), p 4914–4928
47. S. Chatterjee and N. Moelans, A grand-potential based phase-field approach for simulating growth of intermetallic phases in multicomponent alloy systems, *Acta Mater.*, 2021, **206**, p 116630
48. A.m. N.saunders, *CALPHAD(Calculation of Phase Diagrams)-A Comprehensive Guide, Volume 1*, Elsevier Science, 1998
49. S.G. Kim, W.T. Kim, and T. Suzuki, Phase-field model for binary alloys: KKS, *Phys. Rev. E*, 1999, **60**, p 7186–7196
50. S.G. Kim, A phase-field model with antitrapping current for multicomponent alloys with arbitrary thermodynamic properties, *Acta Mater.*, 2007, **55**(13), p 4391–4399
51. S.G. Kim, W. Tae Kim, T. Suzuki, and M. Ode, Phase-field modeling of eutectic solidification, *J. Cryst. Growth*, 2004, **261**(1), p 135–158
52. N. Moelans, B. Blanpain, and P. Wollants, Quantitative analysis of grain boundary properties in a generalized phase field model for grain growth in anisotropic systems, *Phys. Rev. B*, 2008, **78**(2), p 24113
53. N. Moelans, A quantitative and thermodynamically consistent phase-field interpolation function for multi-phase systems, *Acta Mater.*, 2011, **59**(3), p 1077–1086
54. N. Moelans, http://nele.studentenweb.org/docs/parameters.m; http://nele.studentenweb.org/docs/GammaDependence.txt; 2008.
55. M.R. Tonks, D. Gaston, P.C. Millett, D. Andrs, and P. Talbot, An object-oriented finite element framework for multiphysics phase field simulations, *Comput. Mater. Sci.*, 2012, **51**(1), p 20–29
56. A. Mehta and Y. Sohn, High Entropy and Sluggish Diffusion “Core” Effects in Senary FCC Al-Co-Cr-Fe-Ni-Mn Alloys, *ACS Comb Sci*, 2020, **22**(12), p 757–767
57. T. Yang, S. Xia, S. Liu, C. Wang, S. Liu, Y. Zhang, J. Xue, S. Yan, and Y. Wang, Effects of Al addition on microstructure and mechanical properties of Al CoCrFeNi High-entropy alloy, *Mater. Sci. Eng. A* ., 2015, **648**, p 15–22

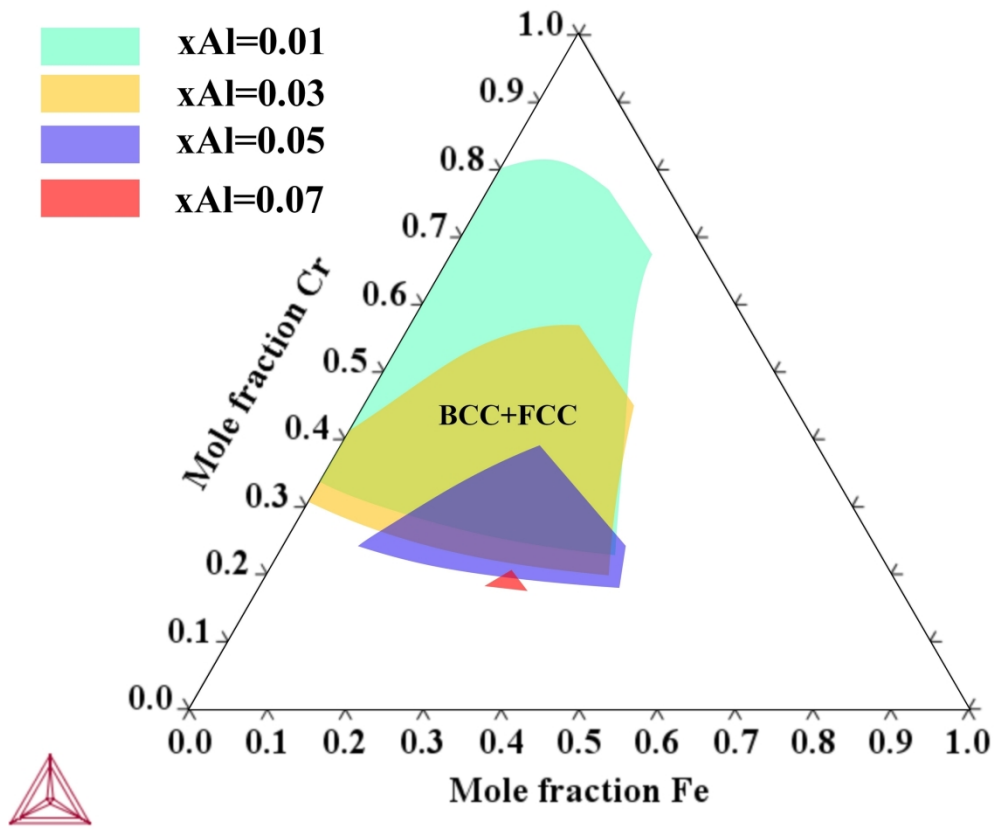

BCC/FCC two-phase region in the ternary sections of the AlCrNiFe phase diagram for fixed amounts of Al

215x179mm (300 x 300 DPI)

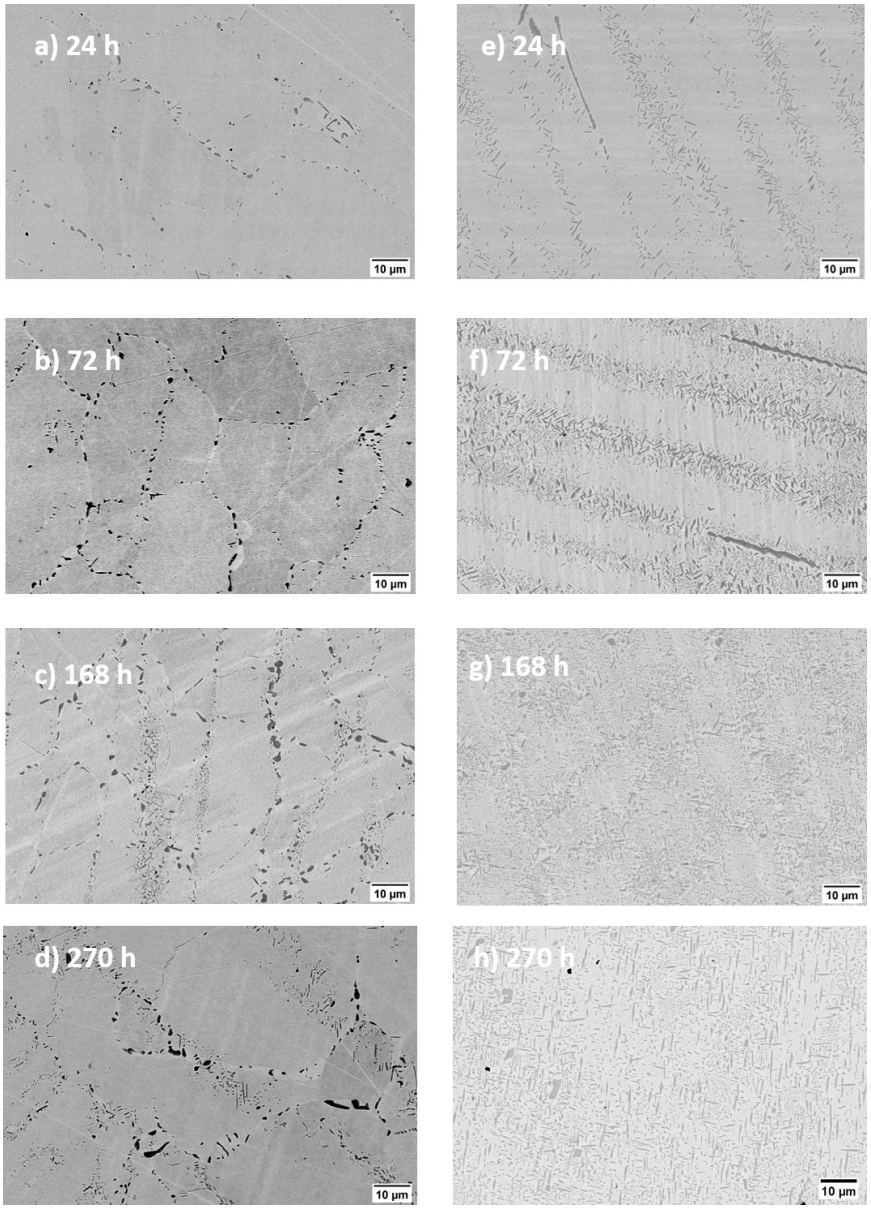

SEM-BSE micrographs showing the evolution of microstructure at 0h,, 72h, 168h and 270h during isothermal aging at 700°C for (a,b,c,d) ternary CrFeNi and (e,f,g,h) quaternary Al-CrFeNi systems.

180x250mm (150 x 150 DPI)

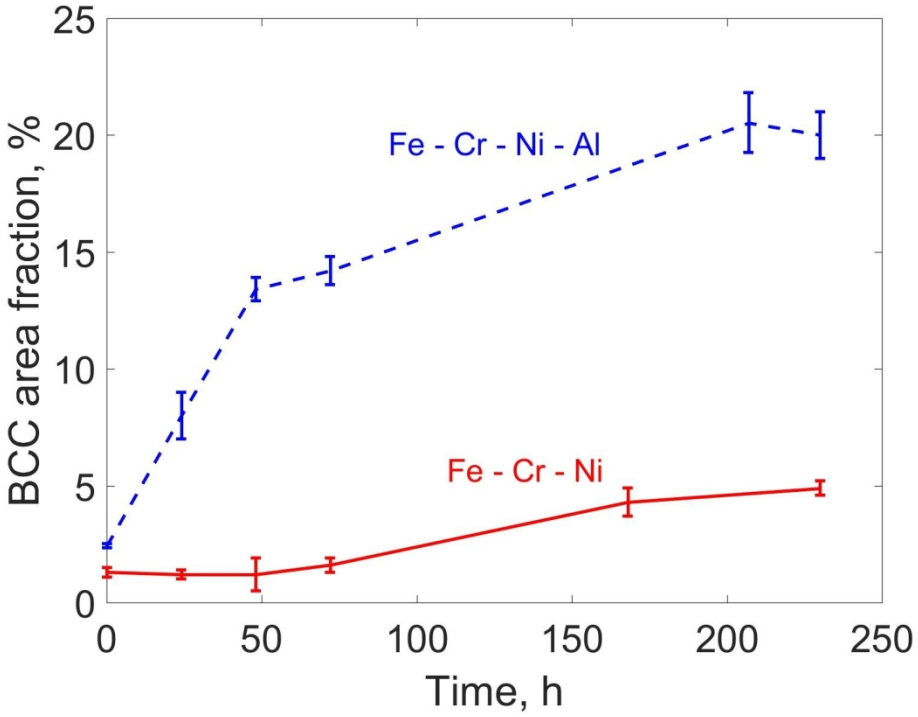

BCC area fraction evolution during isothermal aging at 700°C for quaternary Al-CrFeNi (blue, dotted line) and ternary CrFeNi (red, solid line) alloys.

590x444mm (72 x 72 DPI)

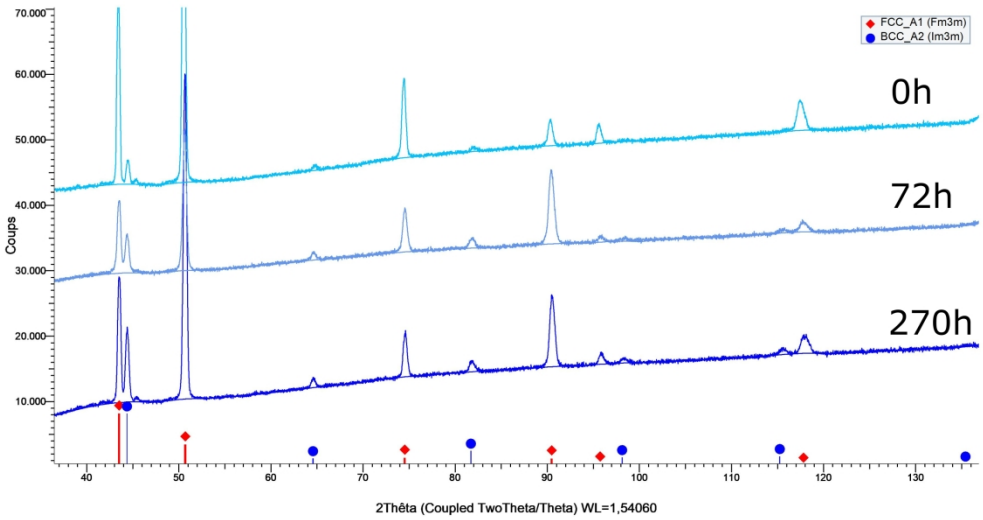

X-Ray diffraction spectra for 0h, 72h and 270h holding at 700°C for Al-CrFeNi alloy showing the presence of a disordered FCC-type (space group Fm3m, highlighted in red) and BCC-type (space group Im3m, highlighted in blue) phase. The intensity of peaks related to BCC phase is increasing for longer holding times at 700°C, which agrees with the increment of volume fraction of the secondary phase.

640x349mm (118 x 118 DPI)

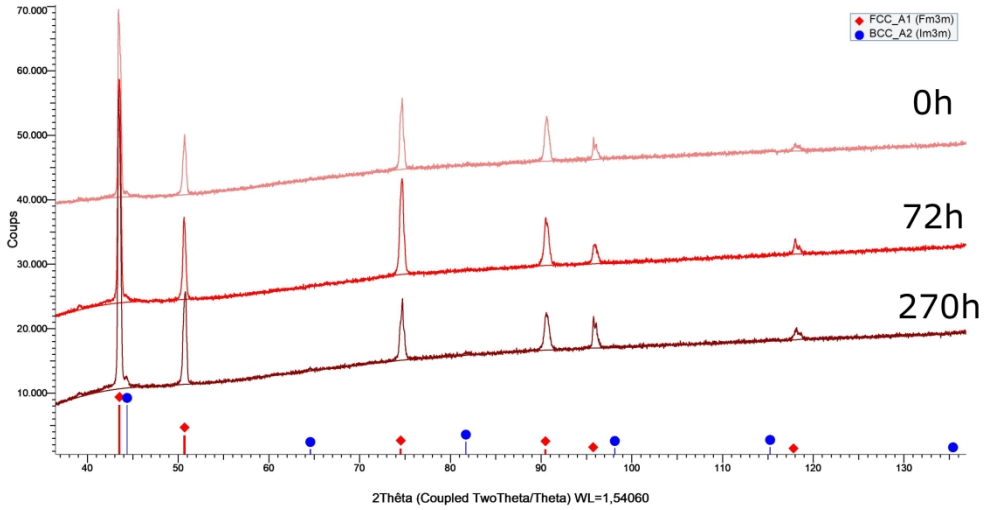

X-Ray diffraction spectra for 0h, 72h and 270h holding at 700°C for Al-free ternary CrFeNi alloy showing the predominance of FCC-type phase in the alloy. A low-intensity peak corresponding to disordered BCC phase (2Theta = 44°) is being detected only after 270h holding at 700°C.

650x341mm (118 x 118 DPI)

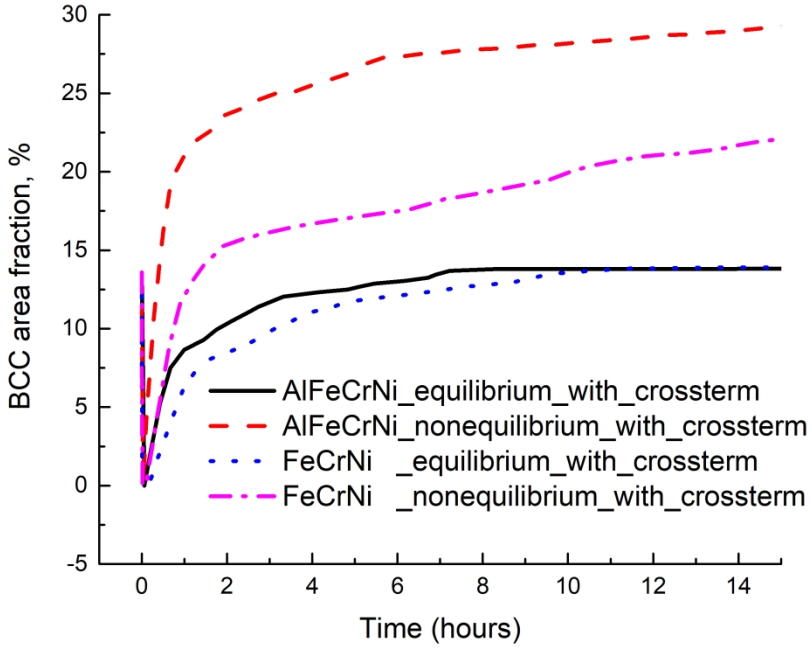

Comparison of the evolution of BCC precipitate area fraction with time in the phase-field simulations for CrFeNi and Al-CrFeNi for an initial structure having the equilibium composition in both the FCC and BCC phase (indicated with 'equilibrium' in the legend) (case EQ in table 2) and an initial structure with FCC composition deviating from the equilibrium (indicated with 'non-equilibrium' in the legend)(case NEQ in table).

272x208mm (300 x 300 DPI)

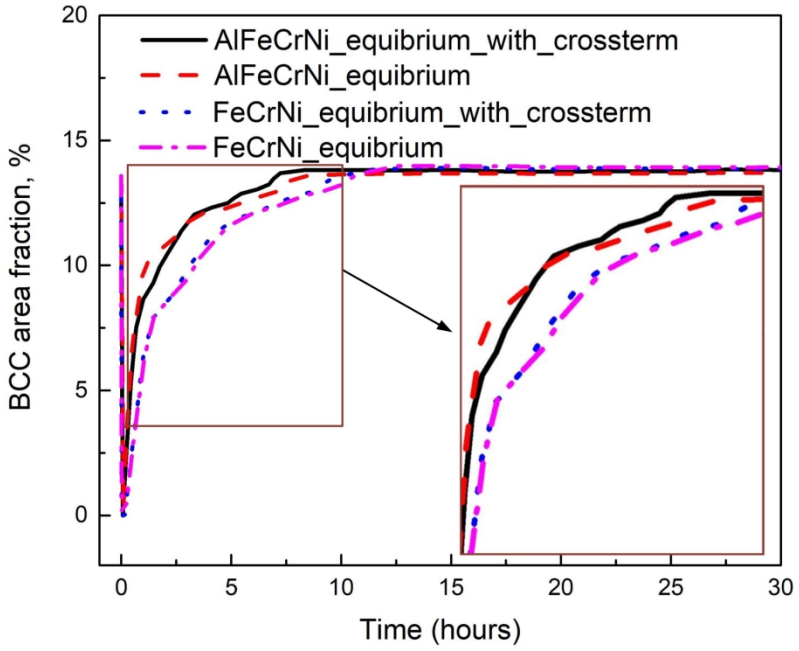

Comparison of the growth area fraction with time of BCC precipitates in simulations (with or without crossterm in the PF calculation) for different alloy systems under same initial conditions.

272x208mm (300 x 300 DPI)

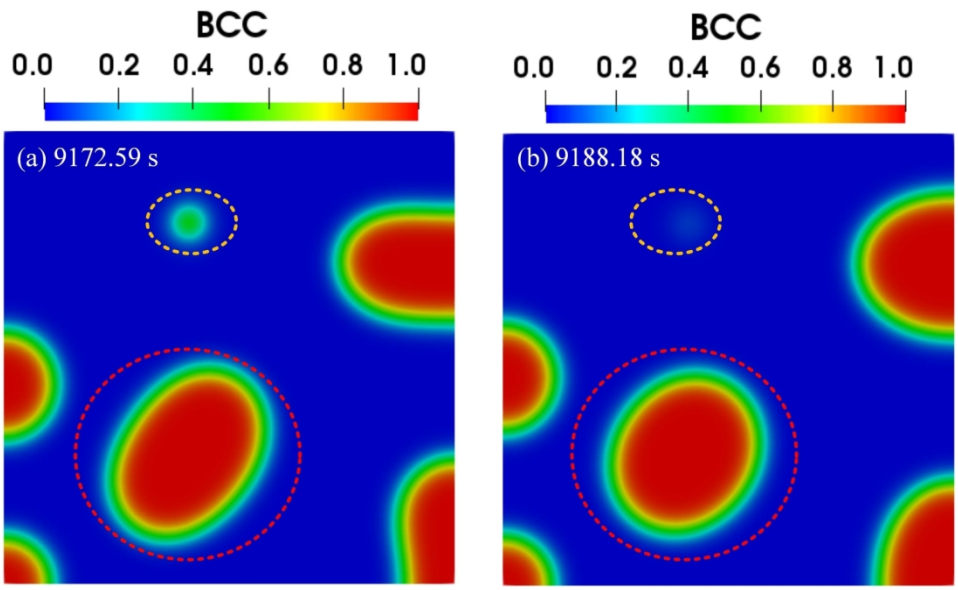

PF simulation images representing the microstructure with BCC precipitates in FCC matrix for the Al-CrFeNi alloy obtained using the model (a) with crossterms and (b) without crossterms, and at similar simulation times, namely (a) 9172.59s and (b) 9188.18s. The initial structure with equilibrium BCC and FCC composition was used.

156x94mm (300 x 300 DPI)

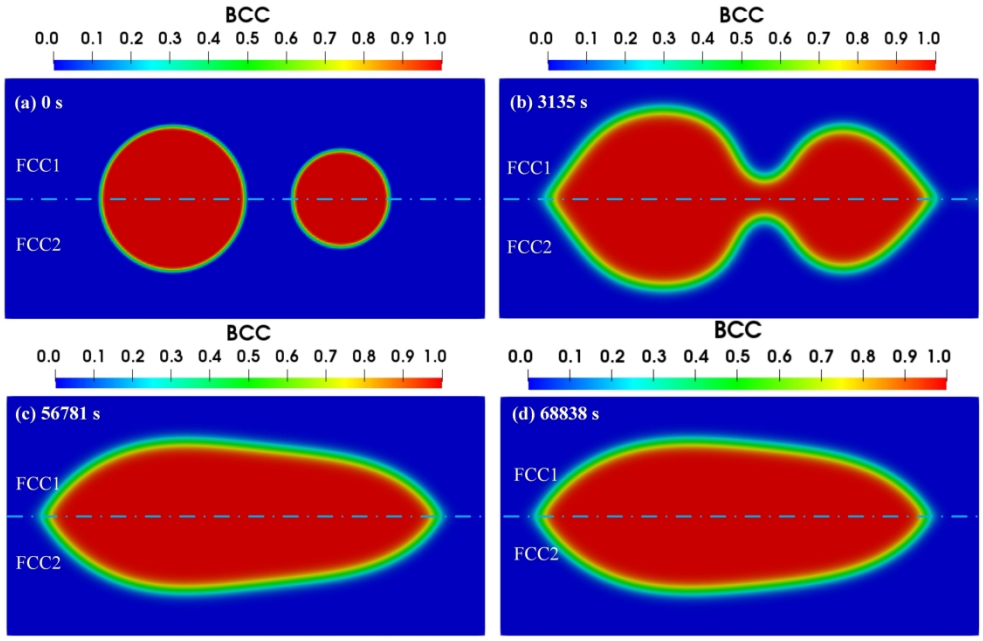

Images of the PF simulation of 2 BCC precipitates growing at an FCC grain boundary in Al-CrFeNi obtained at time frames (a) 0 s (b) 3135 s (c) 56784s (d) 68838 s. The initial microstructure with non-equilibrium composition in the FCC phase (NEQ) is considered.

260x167mm (300 x 300 DPI)

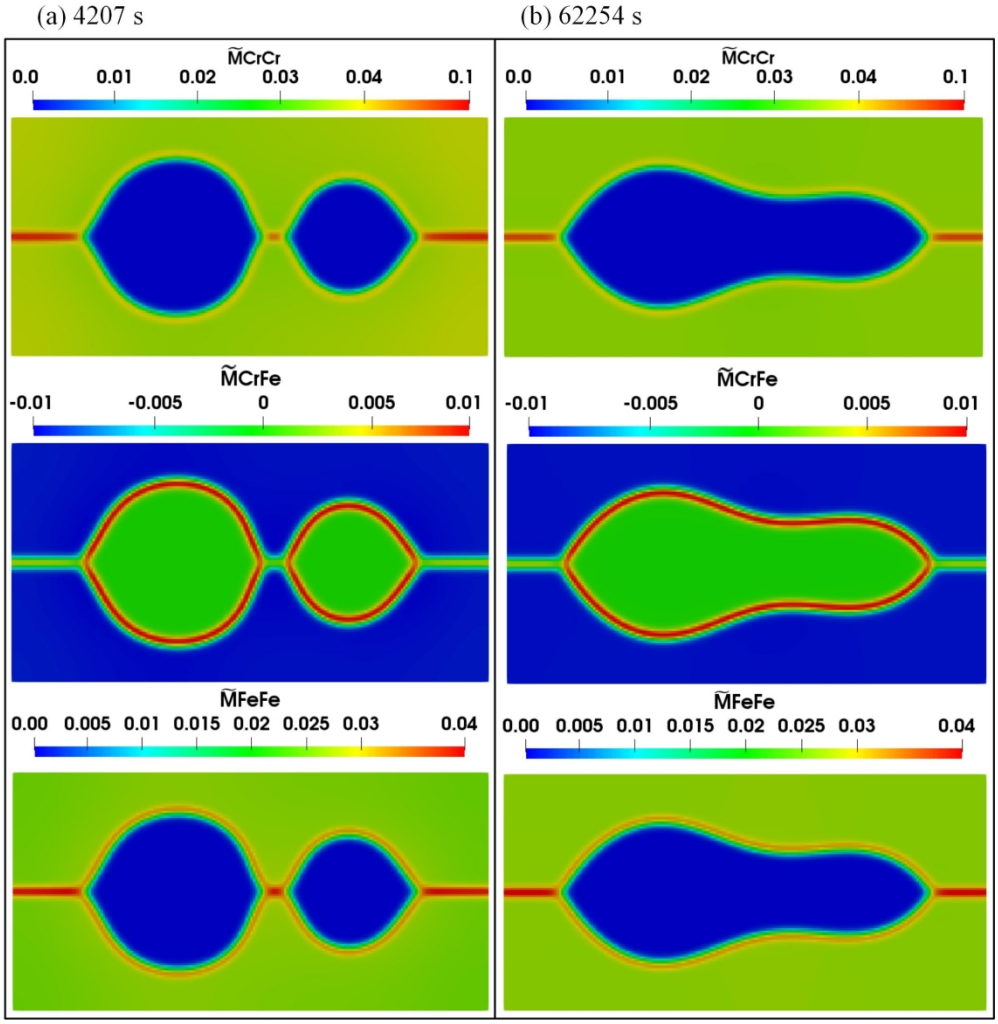

Local mobility values as obtained from the PF simulations for CrFeNi (with initial nonequilibrium composition in FCC phase) at times (a) 4207 s (b) 62254 s.

185x190mm (300 x 300 DPI)

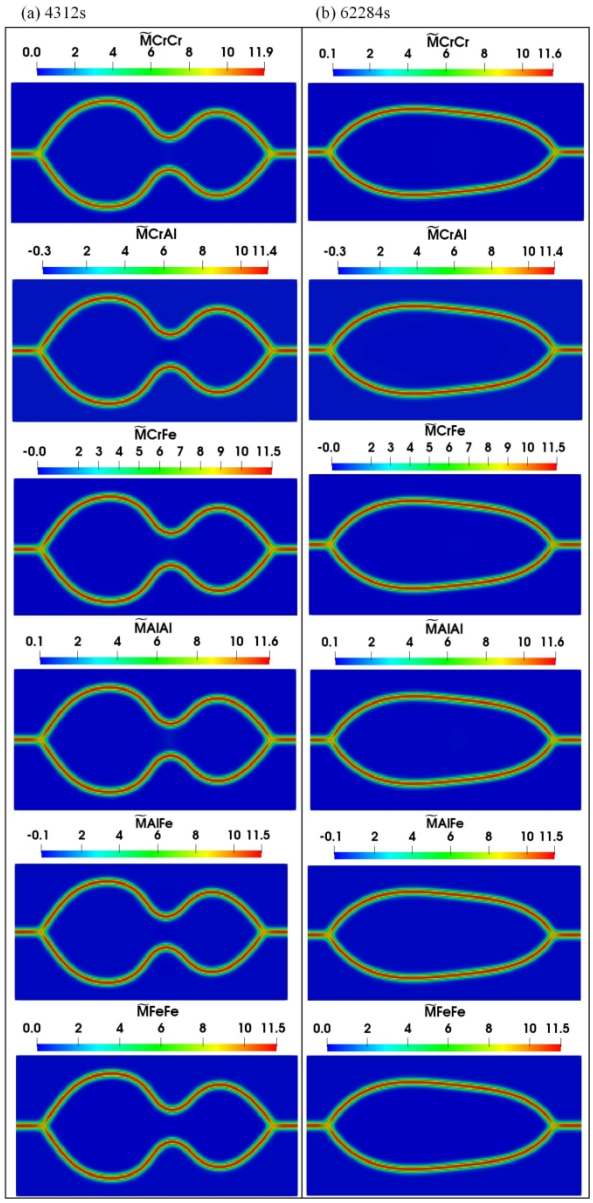

Local diffusion mobility values as obtained from PF simulations for Al-CrFeNi (with initial nonequilibrium composition) at time frames (a) 4312 s (b) 62284 s

143x292mm (300 x 300 DPI)

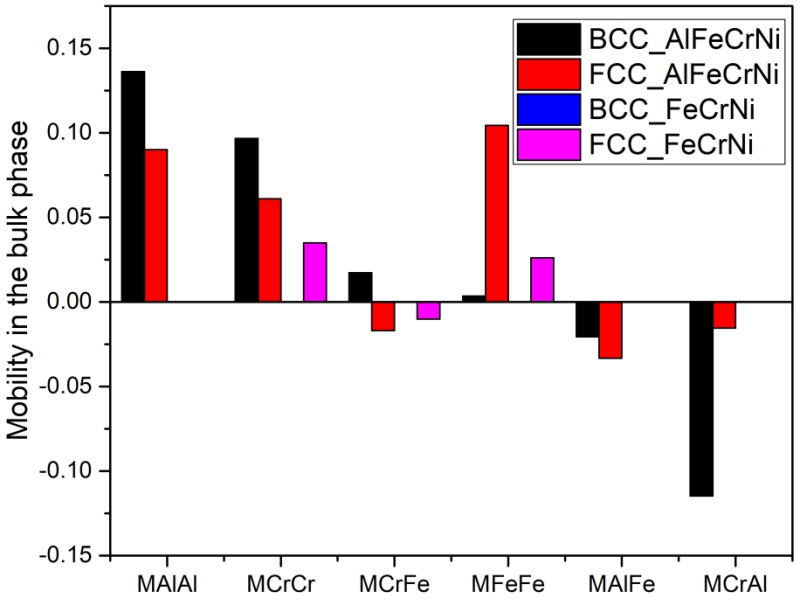

Average dimensionless mobilities in BCC/FCC for Al-CrFeNi (nonequilibrium) at time frames (a) 62284 s and CrFeNi (nonequilibrium) (b) 62254 s

272x208mm (300 x 300 DPI)

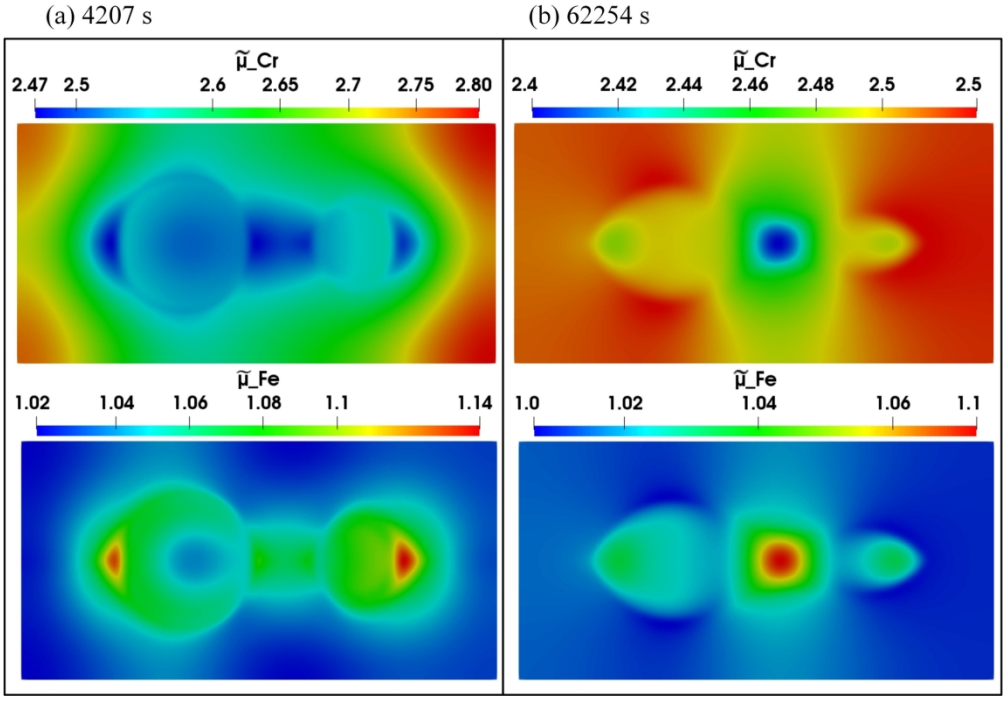

Local values of the diffusion potentials as obtained from PF simulations for CrFeNi (case NEQ in table 2) at time frame (a) 4207 s and (b) 62254 s

185x130mm (300 x 300 DPI)

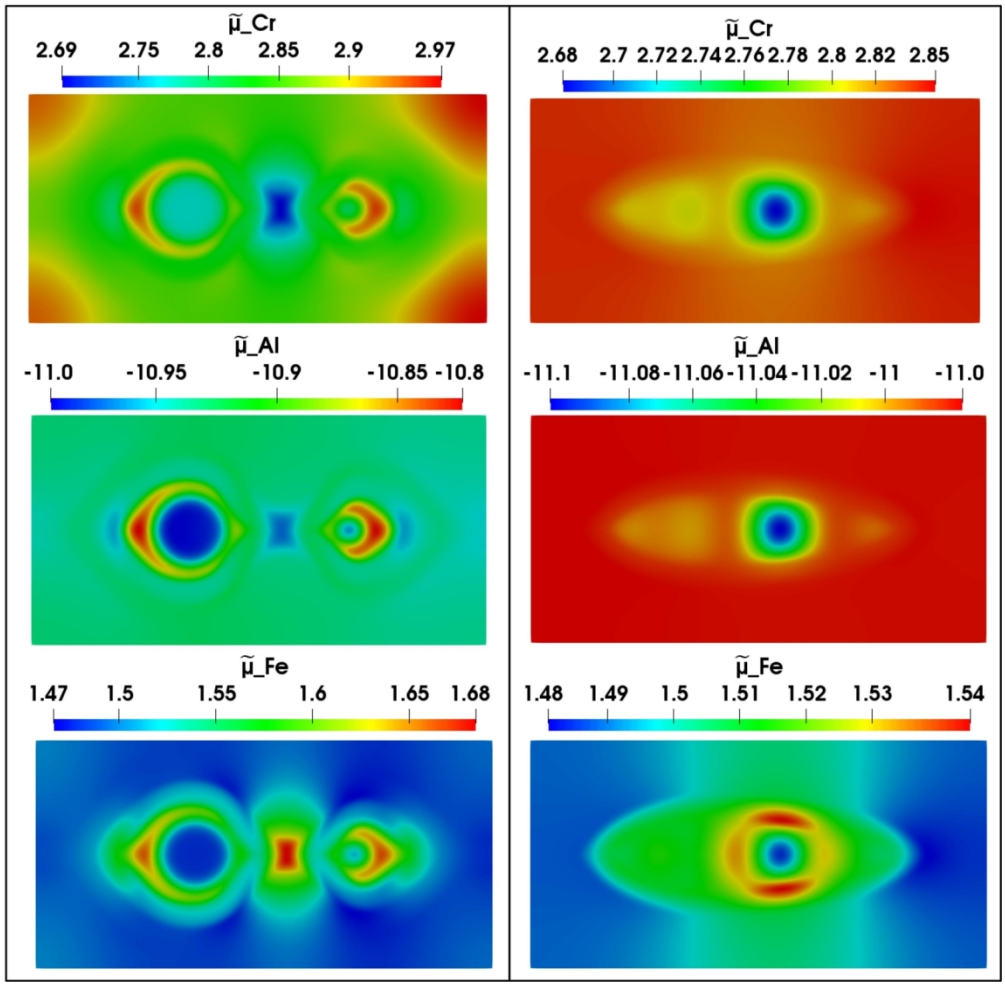

Local values of the diffusion potentials from PF simulations for Al-CrFeNi (case NEQ in Table 2) at time frame(a) 4312 s (b) 62284 s

139x143mm (300 x 300 DPI)

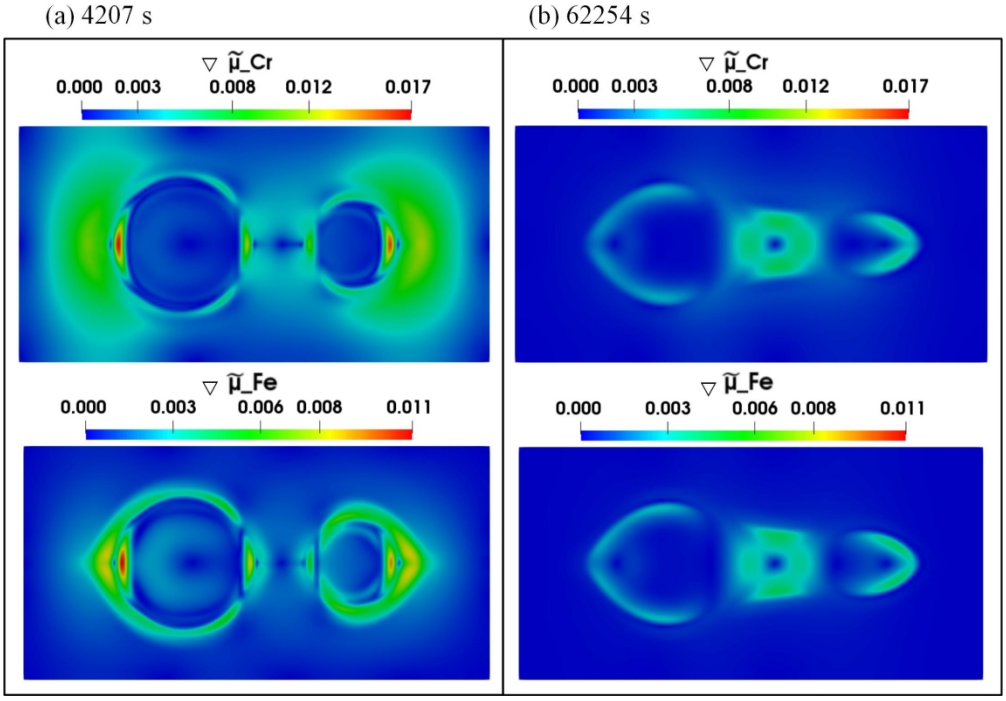

Local values of the gradient of diffusion potentials obtained from PF simulations for CrFeNi (case NEQ in Table 2) at time frame(a) 4207 s (b) 62254 s

185x130mm (300 x 300 DPI)

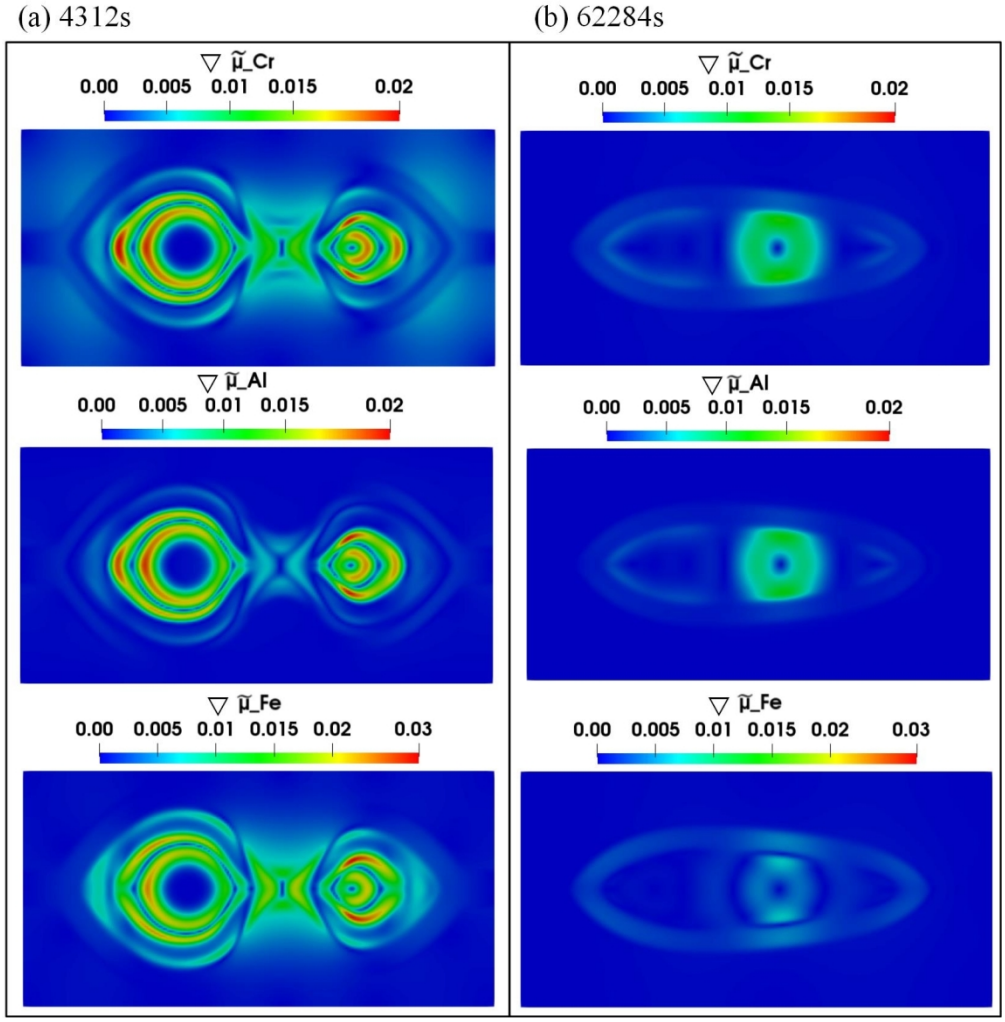

Local values of the gradient diffusion potentials obtained from PF simulations for Al-CrFeNi (case NEQ in Table 2) at time frame(a) 4312 s (b) 62284 s

139x143mm (300 x 300 DPI)

Revision of the manuscript

Influence of 5% Al-additions on the FCC to BCC phase transformation in CrFeNi concentrated alloys

by

X. Zuo, A. Miotti Bettanini, A. Hilhrost, P.J. Jacques, N. Moelans

Reply to the comments of the reviewers and description of the changes made to the manuscript

We would like to express our gratitude to the reviewers for their valuable comments and kind suggestions and the editors' kind help during our paper submission. We modified our paper according to reviewers' comments and suggestions. All the changes are labeled in yellow color in the paper. The detailed responses to all the comments are listed below.

1. ***P11: there exist typos for the equation citation, please check them carefully.***
Yes, the equations have been all carefully checked. And the modifications are labeled in yellow color in the text.

2. ***P12: in L3, 'Where' should be 'where'.***
Yes, the 'Where' has been changed to 'where' in P12.

3. ***L25, P15: in Section 3.2, at the initial stage of PF simulation, the volume fraction of BCC is near to zero, is the curvature effect be caused by the calculated methods or the physical essence? Please provide some references for it to show the correction or the reality.***

The near-zero area fraction of BBC is indeed due to the PF calculation method. For small precipitates, the curvature effect is exaggerated in the PF model due to the diffuse interface. The curvature effect is also present in reality, but it would most probably not lead to a near-zero volume fraction of the BCC. At the initial stage, 50 small (4 nm) BCC precipitates are generated in the calculation domain with a high interface curvature (inverse proportional to the precipitation radius). The atoms from the BCC precipitates tend to diffuse into the matrix due to the curvature effect, resulting in a decline of the BCC area fraction at the initial stage. The shrinkage is however exaggerated in the PF calculation due to the diffuse character of the interfaces and because the initial particles have a particle size smaller than the diffuse interface width. However, this exaggerated shrinkage at the start does only affect the onset of the simulations. The further growth behavior, when precipitates have a larger radius, can be considered as realistic. This shrinkage at the start will not affect the final total area of the BCC precipitate. Moreover, we have taken the same initial conditions for all cases, such that the effect on the comparison of the growth rate between all the studied cases is minimal. We have included a short discussion on this initialization effect in the revised paper.

4. ***P16: from Fig. 7(a), the cross-diffusion terms affect the AlFeCrNi alloy on some extent, while the effect factor of it on the CrFeNi is 0.93 %, how to get this value of 0.93%? Is this value just an error of PF method, rather than the effect of the cross-diffusion terms?***

The value of 0.93% is the maximum deviation on the BCC area fraction between the simulation with and without cross terms for CrFeNi. For each time step, the absolute deviation(|area fraction obtained with cross term-area fraction obtained without cross term|) is calculated (this information is also added in the paper now). We take the maximum of all these values to show the effect from the cross terms, which is relatively small, i.e., 0.93% for the ternary CrFeNi. It is true that the error on the input data, and even the error due to discretization, may be larger than 0.93%. However, since these errors and the simulation conditions are exactly the same for the case with and without cross-terms, we are quite sure that the measured difference is due to the presence or absence of cross-terms in the simulation and not due to other errors from the PF method.

5. ***In Fig. 7(b), the calculated results are given in different times, in which there exists a difference of 16 s. Actually, the calculated time could be controlled, it is better to compare the results at the same calculated time.***

In the simulations, we use adaptive time stepping to save computational costs. We use IterationAdaptiveDT provide by MOOSE (this information is added into the text now). The time step size is based on the difficulty of the solutions, and if fewer iterations are required for the simulation, it will take larger time steps to obtain a solution more quickly. Thus, the calculated results are not available for exactly the same time steps for the different cases.

6. ***Fig. 12b: in (a)4312 s, why does a circular structure appear in gradient diffusion potentials? If the grid density of simulated area is changed, would such structure still exist?***

Fig. 12b shows the gradient of diffusion potential calculated based on the data represented in Fig. 11b. From Fig.11b, it is clear that the diffusion potential at the interface is larger. Therefore, we obtain a circular structure for the gradient in diffusion potentials. We verified that if the grid density is changed, the circular structure still exists. As is seen in the figure below that the circular structure exists when different mesh grid densities(Left: 100*200(409s), Right: 200*400(390s) are used.

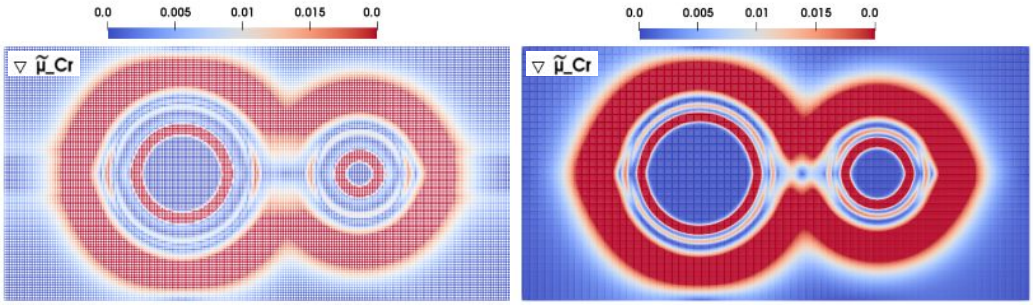

7. ***Fig.2: after a long-time aging at 700 °C, there would certainly exist another kind of sigma phase enriched by Cr and Fe, which has been identified by lots of reported results. The authors should be cautious of the particle distribution on grain boundaries of matrix grains.***

For the the quaternary FeCrNi-5wt.% Al SIGMA phases is not stable at 700°C, which is the temperature we have chosen for the annealing step. Indeed, increasing Al content seems to destabilize SIGMA phase in favour of BCC phase in the Fe-Cr-Ni system. The thermodynamic calculation shown below

(Thermocalc 2021 + TCHEA2 database) confirms the experimental findings. At 700°C, only FCC and BCC are stable. In light of this results, we have chosen the composition specifically to avoid SIGMA phase and to stabilize only FCC and BCC.